

## Cassini microwave observations provide clues to the origin of Saturn's C ring



Z. Zhang<sup>a,\*</sup>, A.G. Hayes<sup>a</sup>, M.A. Janssen<sup>b</sup>, P.D. Nicholson<sup>a</sup>, J.N. Cuzzi<sup>c</sup>, I. de Pater<sup>d</sup>, D.E. Dunn<sup>e</sup>, P.R. Estrada<sup>c,f</sup>, M.M. Hedman<sup>g</sup>

<sup>a</sup> Astronomy Department, Cornell University, Ithaca, NY 14850, USA

<sup>b</sup> Jet Propulsion Laboratory, California Institute of Technology, Pasadena, CA, 91109, USA

<sup>c</sup> Space Science Division, Ames Research Center, NASA, Moffett Field, CA 94035, USA

<sup>d</sup> Astronomy Department, University of California, Berkeley, California 94720, USA

<sup>e</sup> Astronomy Department, Sierra College, Rocklin, CA 95677, USA

<sup>f</sup> SETI Institute, Moffett Field, CA 94035, USA

<sup>g</sup> Physics Department, University of Idaho, Moscow, ID, 83844, USA

### ARTICLE INFO

#### Article history:

Received 9 March 2016

Revised 21 July 2016

Accepted 24 July 2016

Available online 17 August 2016

#### Keywords:

Saturn, rings

Planetary rings

Radar observations

Origin, Solar system

### ABSTRACT

Despite considerable study, Saturn's rings continue to challenge current theories for their provenance. Water ice comprises the bulk of Saturn's rings, yet it is the small fraction of non-icy material that is arguably more valuable in revealing clues about the system's origin and age. Herein, we present new measurements of the non-icy material fraction in Saturn's C ring, determined from microwave radiometry observations acquired by the Cassini spacecraft. Our observations show an exceptionally high brightness at near-zero azimuthal angles, suggesting a high porosity of 70–75% for the C ring particles. Furthermore, our results show that most regions in the C ring contain about 1–2% silicates. These results are consistent with an initially nearly pure-ice ring system that has been continuously contaminated by in-falling micrometeoroids over ~15–90 million years, using the currently accepted value of the micrometeoroid flux at infinity of  $\sim 4.5 \times 10^{-17} \text{ g cm}^{-2} \text{ s}^{-1}$ , and assuming that the C ring optical depth and surface density has not changed significantly during that time. This absolute time scale is inversely proportional not only to the flux at infinity, but also to the amount of gravitational focusing by Saturn the micrometeoroids experience before encountering the rings. We also find an enhanced abundance of non-icy material concentrated in the middle C ring. When assumed to be mixed volumetrically ("intramixed") with water ice, this enhanced contamination reaches a maximum concentration of 6–11% silicates by volume around a ring radius of 83,000 km, depending on the volume mixing model used. This is significantly higher than the inner and outer C ring. As opposed to an intramixing model, we also consider a silicate-core, icy-mantle model to address the fact that silicates may be present in chunks instead of fine powder in the ring particles. Such a model naturally helps to account for the observed opacity distribution. We propose several models to explain the radially varied non-icy material contamination. Our preferred model is that the C ring has been continuously polluted by meteoroid bombardment since it first formed, while the middle C ring was further contaminated by an incoming Centaur, a rocky object torn apart by tides and ultimately broken into pieces that currently reside in the middle C ring. If correct, the spatial extent of the enhanced non-icy material fraction suggests that the Centaur was likely to be captured and integrated into the rings perhaps as recently as ~10–20 million years ago.

© 2016 Elsevier Inc. All rights reserved.

## 1. Introduction

Saturn's rings are the most massive, extensive and diverse ring system in the Solar System, yet despite decades of ground and

spacecraft-based observations (Dougherty et al., 2009; Grossman, 1990; de Pater and Dickel, 1991; van der Tak et al., 1999; Dunn et al., 2002; 2005; Poulet et al., 2003; Nicholson et al., 2008), their origin and age remains a subject of debate. In particular, the small non-icy material fraction, which is related to their origin through source composition and exposure age (Cuzzi and Estrada, 1998), is poorly understood. At first, astronomers predominantly agreed Saturn's rings were primordial (Harris et al., 1984) until

\* Corresponding author.

E-mail address: [zz246@cornell.edu](mailto:zz246@cornell.edu) (Z. Zhang).

observations from the Voyager spacecraft suggested that dynamical considerations necessitated a short ( $\sim 10^8$  yrs) lifetime (Harris et al., 1984; Dones et al., 1991; Goldreich and Tremaine, 1982). A more recent post-Cassini view returns to an ancient origin (Esposito, 2008), but invokes a much more massive pure-ice primordial ring formed via tidal disruption of a Titan-sized, differentiated satellite (Canup, 2010). Yet another recently revisited scenario (Charnoz et al., 2009a) suggests that the cometary flux was so high during the Late Heavy Bombardment (LHB) that several tens of Mimas masses of cometary material may have been brought into Saturn's Hill sphere, and that a fraction of it could have ended in Saturn's Roche zone. In this 'destroyed satellite scenario', it has been recently shown (Charnoz et al., 2009b) that a Mimas-mass moon located  $10^5$  km from Saturn can be disrupted during a LHB type event (Tsiganis et al., 2005) about 700 Myr after the planet's birth (though possibly even later, see Sec. 5.2). The probability for disruption is model dependent, but can be  $> 95\%$  (see Table 3, Charnoz et al., 2009b, and references therein). The abundance and character of non-icy material in Saturn's present-day ring system can help distinguish between these origin scenarios by constraining the composition of source material and, for a given initial composition, estimate the rings' exposure age due to micrometeoroid bombardment (Cuzzi and Estrada, 1998).

The exact composition of Saturn's ring particles remains unclear. Though water ice has long been known as the most prominent component (Cuzzi et al., 1984; Esposito et al., 1984), the single scattering albedos of ring particles are much too low for them to be pure water ice. The rings' spectrum in the visible and near-IR shows strong absorption at near-UV and blue wavelengths leading to a decrease in reflectivity at wavelengths shorter than 0.6  $\mu\text{m}$ . Yet, little is known about the specific makeup of the non-icy, absorbing material that accounts for this observation, the presence of which apparently gives the rings their slightly non-gray, very pale tan or salmon color (Estrada and Cuzzi, 1996). Several investigators have considered a variety of potential UV absorber candidates such as tholins, PAHs, nanophase iron and nanophase hematite in order to match the observed color. Despite the range of materials considered, all of these studies have generally constrained the non-icy fraction to be less than a few percent by mass (Cuzzi and Estrada, 1998; Cruikshank et al., 2005; Morris et al., 1985; Clark et al., 2008). Furthermore, ring photometry has shown that the optically thin C ring and Cassini Division have darker and less red particles than the optically thick A and B rings (Estrada and Cuzzi, 1996), which indicates the presence of varying amounts of unidentified darkening non-icy material with a spectrally neutral color (Smith et al., 1982; Cuzzi et al., 1984; Dones et al., 1993; Poulet et al., 2003; Nicholson et al., 2008). We will later show that the very small amount of reddening material required to give the rings their apparent color in the visible and near IR wouldn't contribute significantly to the microwave observation (Sec. 5.4), and thus it is the presence of some other non-icy material, besides these reddening materials, that determines the intrinsic thermal emission at the wavelength of our interest.

The Cassini RADAR radiometer (Elachi et al., 2004) provides an ideal window through which to study the non-icy material fraction in Saturn's main rings, as it operates at a wavelength where the absorptivity of water ice is negligible compared to that of most non-icy material, and thus the intrinsic thermal radiation from the ring layer is dominated by the non-icy components. Moreover, whereas visible and near-IR spectra are only sensitive to the top millimeter or less of ring particle surfaces, microwave observations are able to sample the bulk of the ring mass. For solid pure water ice particles, microwave radiation from Saturn at 2.2 cm can penetrate as deep as almost 100 m, while the largest particles in the rings are no larger than 10 m (Marouf et al., 2008).

The C ring lies close to Saturn, situated between the D and B rings, and is the darkest of all the main rings. Since first formed, the rings have been continuously darkened by incoming micrometeoroids. In optically thin rings like the C ring, ring particles are sparse and only a fraction of incoming meteoroids actually hit the rings as opposed to merely passing through them. As the rings become optically thicker, a larger fraction of the meteoroids are absorbed by the ring particles until reaching a level of saturation, where none of the incoming meteoroids can pass through. Saturation is reached for an optical depth  $\tau \gtrsim 1$ , while the mass of material to be darkened continues to increase with  $\tau$ . Thus, the optically thin C ring is easier to darken than the optically thicker A and B rings.

It should be noted that many of the structures we see in the C ring lack a satisfactory explanation. Apart from having a profound darkening effect on the rings, micrometeoroid bombardment and transport of their impact ejecta has been shown to explain many aspects of C ring structure (see Estrada et al., 2015), but much of the structure, especially the plateaus, remain enigmatic. A great deal of the mystery of the C ring revolves around the measured ring opacity (see Sec. 5) which can be associated with the particle size distribution. A complete radial profile of the C ring opacity is lacking, but observations suggest that the particle size distribution in the C ring differs across the ring and within different ring regions (e.g., Marouf et al., 2008; Cuzzi et al., 2009; Colwell et al., 2011, 2012) which further complicates efforts to explain the observed structure. Though our analyses in this paper are not meant to address the specifics of C ring structure, we do advance a compelling model to explain the anomalously low opacity (and thus structure) in the middle C ring (Sec. 5.2).

Despite the complexities associated with the particle size distribution across the C ring, the C ring has a lower optical depth and smaller particle albedo than the A and B rings, so one would expect the C ring to have the highest abundance of non-icy material and hence be the ideal place for studying the rings' contamination history. It had been noted as early as Voyager that the presence of some then as-of-yet unknown non-icy component is required to account for the regional and local color variations in ring color (e.g., Smith et al., 1982); however, because previous radio-wave observations have been limited by resolution and sensitivity, no detailed C ring non-icy material fraction has been reported until now. In this work, we determine the non-icy fraction and attempt to constrain candidate materials from the brightness temperature profile of the C ring obtained from analysis of Cassini RADAR observations with resolutions as high as  $\sim 2000$  km. The observed flux is composed of scattered Saturn radiation and intrinsic thermal emission, the latter being directly related to the non-icy material fraction.

In Section 2 we give an overview of Cassini Radiometry observations of the rings and describe the calibration process and the resulting brightness temperature map. In Section 3, we present the method we use to model the microwave scattering and emission in the rings. We also list the ring parameters that determine the simulated brightness temperature. In Section 4, we compare simulated brightness temperatures from the model with Cassini observations, vary the ring properties, and search for the best-fit parameters. In section 5, we discuss the implication of our results and suggest possible ring origin scenarios that could explain our findings. In Section 6, we summarize our conclusions on the C ring particle porosity, the radially varied non-icy material fraction profile and their implications for the rings' origin and age.

## 2. Observations & deconvolution

The Cassini RADAR instrument (Elachi et al., 2004) scanned Saturn and its rings at 2.2 cm wavelength on twelve occasions

**Table 1**  
Cassini Radiometry Data Set.

Occasion	Request Name	Scan Type	Calendar Date	Distance ( $R_S$ )	Opening Angle (degree)
Rev028_HIGH	RADAR_028RI_PO1RINGS002_PRIME	High-resolution spoke scan	2006-253T01:00:00–2006-253T06:00:00	6.7	-24.5~–23.3
Rev028_LOW	RADAR_028RI_045MATCH001_PRIME	Low-resolution map scan	2006-254T08:00:00–2006-254T11:30:00	19.2	-22.2~–21.9
Rev038_1_LOW	RADAR_038RI_038MATCH1001_PRIME	Low-resolution map scan	2007-027T16:36:00–2007-028T02:36:00	24.4	-22.5~–18.3
Rev038_2_LOW	RADAR_038RI_038MATCH2001_PRIME	Low-resolution map scan	2007-035T20:52:00–2007-036T05:22:00	21.9	-20.8~–15.5
Rev039_LOW	RADAR_039RI_39R1MATCH001_PRIME	Low-resolution map scan	2007-054T13:11:00–2007-054T19:22:00	24.1	-24.5~–21.7

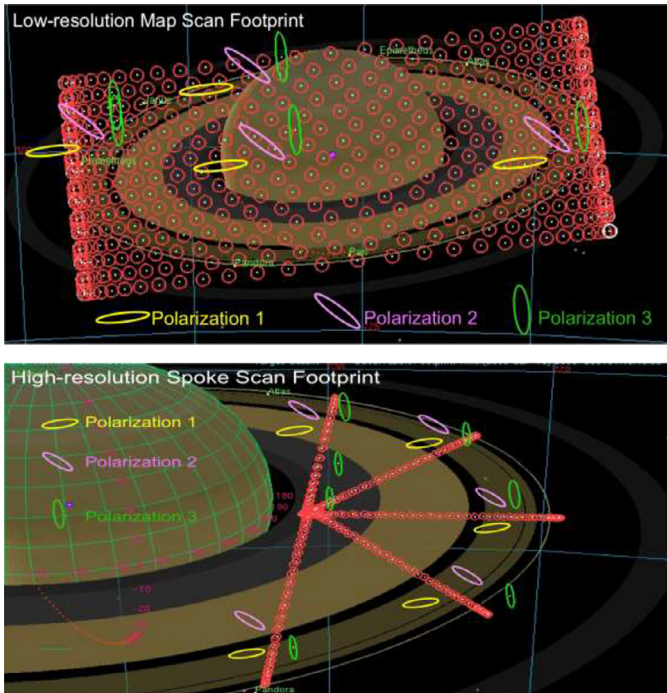


**Fig. 1.** Footprint of Cassini Radar on the rings during low-resolution map scan (upper panel) and high-resolution spoke scan (lower panel) [figures from the Cassini RADAR team page]. Small red circles represent the half-power beam width of the Cassini Radar Beam 3 and show the observation footprints on the rings. Beam 3 is the central Radar beam used for radiometry. The major axes of the ellipses show the linear polarization orientations; polarization 1 (yellow), horizontal to the ring plane; polarization 3 (green), ~20° to the ring plane normal, roughly aligned with the projection of the ring plane normal in the figure; and polarization 2 (purple), which lies in between polarizations 1 and 3. (For interpretation of the references to colour in this figure legend, the reader is referred to the web version of this article.)

during its prime mission between Dec 2004 and Oct 2008. There are two categories of radiometric observations of Saturn's rings: low-resolution map scans from a distance of  $\sim 20 R_S$  (where  $R_S = 60,330$  km is Saturn's radius) and high-resolution "spoke scans" (not related to the fuzzy features seen in the B ring) from a distance of  $\sim 5 - 8 R_S$ . The map scan "footprints" (**Fig. 1 upper panel**, red circles) cover all of the main rings at all azimuthal angles. The projection of the line connecting Saturn center and the spacecraft onto the ring plane lies at zero degree azimuth, and the azimuthal angle increases anti-clockwise in the ring plane. At small azimuthal angles, the observed ring regions occult Saturn. These observations are comparable to stellar and radio occultations except that the light source is due to the planet's radiation. On the other hand, high-resolution spoke scan footprints (**Fig. 1 lower panel**, red circles) only cover the main rings at five distinct azimuthal angles where the rings are not occulting Saturn. While map scans reveal the complete angular scattering profile, spoke scans show finer radial structures. Five of these occasions (four low-resolution maps and one set of high-resolution spoke scans) were collected when the ring plane had the largest ring opening angle of about  $-20^\circ$

and thus they have the best resolution. In this work, we investigate these five datasets as listed in **Table 1**.

The Cassini Radar has a main beam size of  $0.36^\circ$  in angular diameter (full width at half maximum [FWHM] power). As the main-beam projects onto the ring plane, the resolution in the direction perpendicular to the line-of-sight equals the angular diameter multiplied by the observer-target distance, while the resolution along the line-of-sight is elongated by a factor  $(\sin |B|)^{-1}$ , where  $B$  is the opening angle. In high and low resolution cases with a  $\sim 20^\circ$  ring opening angle, the radial resolution is about  $\sim 2000$  km and  $\sim 8000$  km, respectively, in the direction perpendicular to Cassini's line-of-sight, and  $\sim 6000$  km and  $\sim 24,000$  km, respectively in the direction parallel to Cassini's line-of-sight. For each occasion, the data are collected at three different linear polarization orientations: polarization 1, horizontal to the ring plane; polarization 3,  $\sim 20^\circ$  to the ring plane normal; and polarization 2, which lies in between polarizations 1 and 3. As described below, each polarization is calibrated independently.

While this data set presents several advantages, such as the low microwave absorptivity of water ice and a wavelength comparable to the size of the most abundant ring particles, it is also very challenging to process. This is because Saturn and its rings are extended targets that require combining a large number of measurements to obtain full coverage. More importantly, each measurement of antenna temperature is the convolution of the radiometer's broad gain pattern and the brightness temperature of all targets in the field of view (Janssen et al., 2009). The antenna temperature  $T_a$  is given by

$$T_a = \int_0^{2\pi} \int_0^{\pi} T_b(\theta, \phi) G(\theta, \phi) \sin \theta d\theta d\phi. \quad (1)$$

where  $(\theta, \phi)$  is the angular deviation from the beam center,  $T_b(\theta, \phi)$  is the brightness temperature in the direction of the solid angle element  $\sin \theta d\theta d\phi$ , and  $G(\theta, \phi)$  is the gain of the antenna. The gain pattern of the Cassini RADAR was measured in-flight by Janssen et al. (2009), and consists of an asymmetric near-Gaussian main beam (FWHM of  $0.36^\circ$ ) with extensive sidelobes that, on average, drop to  $\sim 35$  dB ( $10^{-3.5}$ ) within  $\sim 2^\circ$  of beam center. The sidelobes outside  $2^\circ$ , which extended as far as  $60^\circ$ , were never measured in the ground calibrations, but were solved for as a byproduct of mapping Titan (Janssen et al., 2016). The gain is normalized such that:

$$\int_0^{2\pi} \int_0^{\pi} G(\theta, \phi) \sin \theta d\theta d\phi = 1. \quad (2)$$

Radiometer processing requires two primary tasks: (1) relate the normalized counts obtained by the radiometer to antenna temperature, and (2) remove beam sidelobe contributions to convert measured antenna temperature to target brightness temperature in the direction of the beam axis. In order to obtain values of  $T_b$ , the contribution to the signal from the sidelobes must be removed from each observation. To remove the sidelobe contributions from measurements of Saturn's rings, we developed an iterative adaptation of the successful calibration and sidelobe removal algorithms developed for Titan (Janssen et al., 2009; 2016) and Saturn (Janssen et al., 2013). Because Saturn is an order of magnitude brighter than the rings and always sits in the sidelobes,

a more complex processing scheme was required to handle the sidelobes for ring observations.

The observed antenna temperature  $T_a$  is derived from the response to hot and cold reference targets observed by the antenna, while a reference load tracks relative gain variations. The conversion from normalized counts on the sky  $N_{\text{sky}}$  to  $T_a$  is given by (Janssen et al., 2009)

$$T_a = (N_{\text{sky}}/A) - T_{\text{sys}}. \quad (3)$$

where  $T_{\text{sys}}$  is the system baseline offset due to the receiver noise temperature and the physical temperature of the reference load, and  $A$  is the receiver gain. Both the baseline and gain drift with time due to the aging of receiver components. We use the gain calibration and drift factors described in Janssen et al. (2013), which include a time-dependent component allowing for linear gain drift

$$T_{\text{acorr}} = T_a \cdot (1 - 0.004t) \cdot F_{\text{corr}}. \quad (4)$$

where  $t$  is the time in years since the start of September 2005.  $F_{\text{corr}}$  is the gain correction accounting for two factors: 1) gain calibration adjustment for converting original Titan calibration (Janssen et al., 2009) to September 2005 Saturn calibration (Janssen et al., 2013); 2) the reduction in reference Titan brightness of 92 K by a factor of 0.994 at the top of the atmosphere (Janssen et al., 2016).

After deriving calibrated measurements of  $T_a$ , it remains to obtain the brightness temperature  $T_b$  in the direction of the beam center. The main objective of this task is to remove contributions that are distant from the beam axis in order to obtain a best estimate of the on-axis brightness. We begin by separating the antenna temperature into the cold sky baseline  $T_{\text{zero}}$  and the relative antenna temperature  $T'_a$  with respect to the cold sky:

$$T_a = T_{\text{zero}} + T'_a. \quad (5)$$

The cold sky baseline  $T_{\text{zero}}$  is determined from excursions off-source at the end of every scan. By linearly interpolating baseline estimates with time between adjacent cold sky observations, we obtain the offset for each point.

The antenna gain pattern can be written as the sum of a main beam and a sidelobe pattern (Janssen et al., 2009):

$$G(\theta, \phi) = G_{\text{mb}}(\theta, \phi) + G_{\text{sl}}(\theta, \phi). \quad (6)$$

Therefore, the antenna temperature  $T_a$  in Eq. (1) can now be written as:

$$T_a = T_{\text{zero}} + \int_0^{2\pi} \int_0^{\pi} (T_b(\theta, \phi) - 2.7K) \cdot (G_{\text{mb}}(\theta, \phi) + G_{\text{sl}}(\theta, \phi)) \sin \theta d\theta d\phi. \quad (7)$$

where 2.7 K is the CMB brightness temperature when looking at cold sky. Our desired result is the average brightness in the main beam:

$$\bar{T}_{\text{mb}} = \frac{\int_0^{2\pi} \int_0^{\pi} T_b(\theta, \phi) G_{\text{mb}}(\theta, \phi) \sin \theta d\theta d\phi}{\int_0^{2\pi} \int_0^{\pi} G_{\text{mb}}(\theta, \phi) \sin \theta d\theta d\phi}. \quad (8)$$

On the other hand, the average brightness in the sidelobes is given by

$$\bar{T}_{\text{sl}} = \frac{\int_0^{2\pi} \int_0^{\pi} T_b(\theta, \phi) G_{\text{sl}}(\theta, \phi) \sin \theta d\theta d\phi}{\int_0^{2\pi} \int_0^{\pi} G_{\text{sl}}(\theta, \phi) \sin \theta d\theta d\phi}. \quad (9)$$

Combining Eq. (7) with (8) and (9) yields the mean brightness temperature in the main beam:

$$\bar{T}_{\text{mb}} = \frac{1}{1-b} [T_a - T_{\text{zero}} - b(\bar{T}_{\text{sl}} - 2.7K)] + 2.7K. \quad (10)$$

where  $b = \int_0^{2\pi} \int_0^{\pi} G_{\text{sl}}(\theta, \phi) \sin \theta d\theta d\phi$ .

Once the brightness temperature distribution is sufficiently well known, we can use Eq. (10) to estimate and remove the fractional sidelobe contributions. Due to the broad gain pattern, Saturn is always sitting in the sidelobes. We use the modeled microwave brightness for Saturn, which varies with emission angle, derived in Janssen et al. (2013) when calculating their sidelobe contributions, and 2.7 K for the cold sky. However, the brightness distribution in Saturn's rings, which also contributes to the sidelobes, is measured as part of the scan as well. Therefore, a two-dimensional reference model of the brightness temperature of Saturn's rings, assumed to be a function of azimuthal angle (the spacecraft projection on the ring plane lies at zero azimuthal angle) and radius (distance from Saturn center), is required for sidelobe removal. In order to obtain this model, which is essentially our desired measurement, we make an initial guess, then iterate the solution and update the reference model until it converges to a minimum RMS residual error between the modeled and observed antenna temperatures for a given set of observations. This iteration step is the primary modification between the processing procedure proposed herein and the processing algorithms described in Janssen et al. (2009), and Janssen et al. (2013).

Our initial guess for the reference model is a uniformly bright ring system at 7 K with *a priori* knowledge of the innermost (74,510 km) and outermost (136,780 km) radii of the C and A rings. Considering that the D ring (interior to the C ring) has very low optical depth and is barely observable in microwave regions, its sidelobe contributions can be neglected. The sidelobe contributions from the F ring (exterior to the A ring) are also generally ignored for the same reasons in addition to being quite narrow. We obtain modeled antenna temperatures by convolving the beam pattern with the brightness temperature reference model for each observation point. We then subtract the antenna temperature model from the calibrated and baseline-adjusted observed antenna temperatures to produce a residual map. These residuals are then added back into the model and used as a new reference model in the next iteration. We continue this process until reaching convergence, such that further updating of the input ring model does not result in further reduction of the residuals.

We now have enough information to generate a full-scale 2D brightness map model when calibrating data from low-resolution map scans, since they cover all radii and azimuths. However, for the high-resolution Rev028\_HIGH, we only have five spoke scans at five distinct azimuthal angles (see Fig. 2, upper panel), which does not provide enough information to generate a full map. To address this, we generated a 1D brightness temperature model (brightness vs ring radius) for each spoke scan (see Fig. 2, lower panel) and interpolated between them to get a full 2D map. This iterative calibration process is not very sensitive to initial model conditions. Even when starting with a totally uniform ring model, we obtain a minimum RMS residual of ~0.2 K after typically ~5 iterations, which is about 2% of the observed brightness temperature (see Fig. 3). Different initial models converge to the same output ring brightness map after a similar number of iterations which gives us confidence in our approach. We note that during our calibration process, there was an issue caused by a beam offset, especially for the low-resolution scans when the observer-target distance is large. We readily resolved this issue by applying an appropriate antenna pointing correction (see Appendix A for details).

Fig. 4 shows the output of our calibration and processing applied to a low-resolution map scan of Saturn's rings obtained during Rev038\_2\_LOW. Within low-resolution map scans, observations with the main beam where the rings occult Saturn's disk are referred to as "occultation" data. These data are similar to stellar occultations observed by Voyager and Visual and Infrared Mapping Spectrometer (VIMS), except that the source of radiation is the planet itself. Fig. 5 (upper panel) shows the radial

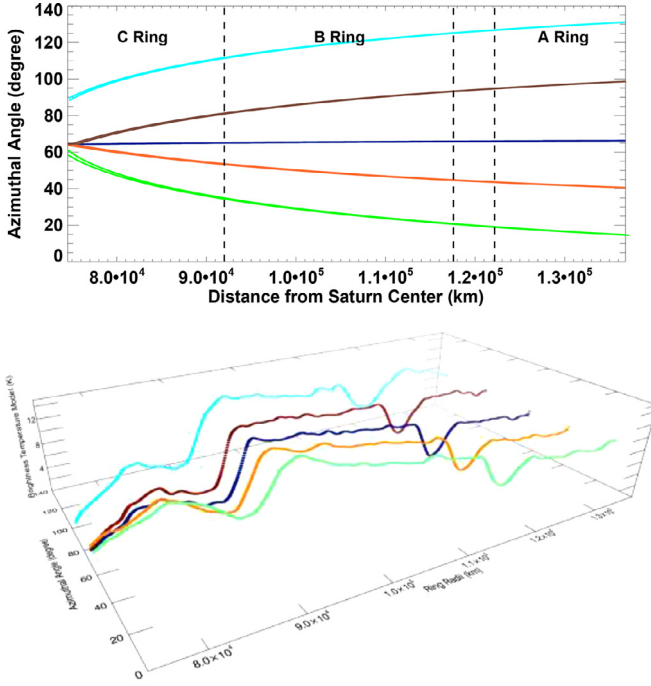


**Fig. 2.** High-resolution spoke scans for Rev028\_HIGH (Polarization 2); Upper panel: the C ring, B ring, Cassini Division (lying between the B and A rings) and A ring azimuthal angles vs ring radii covered. Data are collected at five distinct azimuthal angles. Lower panel: 1D brightness temperature model (brightness vs ring radius) for each spoke scan at one iteration. The colors correspond to the ones in the upper panel. We then interpolated between them to generate the 2D reference model. (For interpretation of the references to colour in this figure legend, the reader is referred to the web version of this article.)

brightness temperature profile of the deconvolved occultation data in Rev038\_2\_LOW. The brightness temperatures at any given ring radius are scattered because we have combined observations at various azimuthal angles. Fig. 5 (lower panel) shows the coverage of ring radius and azimuthal angles of the occultation observations shown in the upper panel. They are part of the Rev038\_2\_LOW scan path (see Fig. 1 upper panel for an example of low-resolution map scan paths), where the main beam falls on ring regions that are occulting Saturn. We note that there are fine structures of about  $\sim 1/10$  of our beam resolution, which are actually not resolved radial structure but are correlated with the azimuthal angles these data were collected at. These small bumps (as can be seen in the red box, upper panel) in the brightness temperature profile were collected at azimuthal angles approaching zero (red box, lower panel). Their increased brightness is because the C ring particle scattering phase function increases with decreasing scattering angle near zero azimuth (see Sec. 3.4).

Fig. 6 shows the brightness  $T_b$  profile vs. distance from Saturn center after processing the Rev028\_HIGH high-resolution spoke-scans. All of these observations are collected when the rings are not occulting Saturn, at azimuthal angles larger than  $20^\circ$ . Going from the C ring to B ring and then to A ring, the distance from Saturn increases, and hence the planet's angular size decreases as seen from Cassini's vantage point. The dashed curves in Fig. 6 illustrate the decreasing trend of incoming radiation from Saturn as the observation point moves further away from Saturn center. While  $T_b$  follows the trend of incoming Saturn radiation in most parts of the rings, the distinct bump (with a peak at  $\sim 83,000$  km) in the C ring's brightness is too large to be attributed simply to optical depth variation (see Sec. 4), which suggests some unusual properties. We will show that this effect may result from a

radially variable increase in non-icy material fraction that produces an extra amount of intrinsic thermal emission.

In Fig. 6, we also see significant variations between spoke scans at different azimuthal angles in the C and A rings, as opposed to the consistent agreement seen in the B ring. In the C ring, the one especially high scan (green curve) was collected at the smallest azimuthal angle ( $\sim 40^\circ$ , see the green curve in Fig. 2, upper panel). Because the particle size distribution in the C ring is characterized by a steep power law ( $q = 3.15$ , see Sec. 3.3) with a minimum size ( $a_{\min} = 0.4$  cm) an order of magnitude smaller than our wavelength, their scattering behavior can be approximated by Mie scattering, which is forward directed. Therefore, a larger amount of light will be scattered into smaller azimuthal angles. However, in the A and B rings, non-sphericity and close-packing effects become important, and therefore ring particles scatter light more isotropically (see Sec. 3.4). This is why in the B ring, the brightness of spoke scans at different azimuthal angles are quite similar. On the other hand, the difference between different spoke scans in the A ring is caused by the self-gravity wake structures (Nicholson and Hedman, 2010). For this set of high-resolution spoke scans, the spacecraft only scans the west side of the ansae. The spoke scan with the highest brightness in the A ring (light blue curve) was collected at the largest azimuthal angle ( $\sim 130^\circ$ ), which is consistent with previous VLA observations (Dunn et al., 2004) (see light blue curve in Fig. 2, upper panel).

We also investigated the polarization effects (Grossman et al. 1989, van der Tak et al. 1999) in the data. In the C ring, the observed light is most polarized at  $\sim 80^\circ$  azimuth, where the degree of linear polarization reaches its maximum value of  $\sim -20\%$  (negative for linear polarization perpendicular to the scattering plane). The brightness in the B and A rings is less polarized, with the value of the degree of linear polarization less than 8%. Due to the complicated and widespread directions of the incident Saturn radiation, it is very difficult to simulate the polarization effect. Although our model (see Sec. 3) cannot deal with polarization, fortunately the non-icy material fraction and the amount of thermal emission in the C ring, which are the main focus of this work, don't depend on the direction of the polarization. Therefore, we combine the data from all three polarizations and treat them as unpolarized. However this polarization variation in observed brightness will have the effect of increasing the uncertainty of our final non-icy material fraction profile.

### 3. Brightness temperature model

The observed brightness temperature  $T_b$  is composed of four components: (1) directly transmitted Saturn radiation (which exists in occultation data only); (2) scattered Saturn radiation; (3) intrinsic thermal emission; and (4) cosmic microwave background (CMB) contributions.

To simulate the observed brightness we use the Monte-Carlo-based photon counting code *SimRings* (Dunn et al., 2002). *SimRings* is able to deal with multiple scattering within the ring layer (where the light source is from extended Saturn emission) and derive the amount of directly transmitted Saturn radiation, scattered Saturn radiation and the intrinsic thermal emission that arrives at the observer. *SimRings* requires knowledge of the ring particles' composition and size distribution, which determines the scattering phase function and absorption rate, and the local optical depth. The amount of directly transmitted Saturn radiation merely depends on the ring's optical depth, the viewing angle and whether the ring is occulting Saturn's disk at the observation point, while the rings' intrinsic thermal emission mainly depends on the non-icy material fraction since the emissivity of water ice at 2.2 cm is negligible. Considering that the imaginary part of the dielectric constant of water ice is 3 orders of magnitude smaller than that

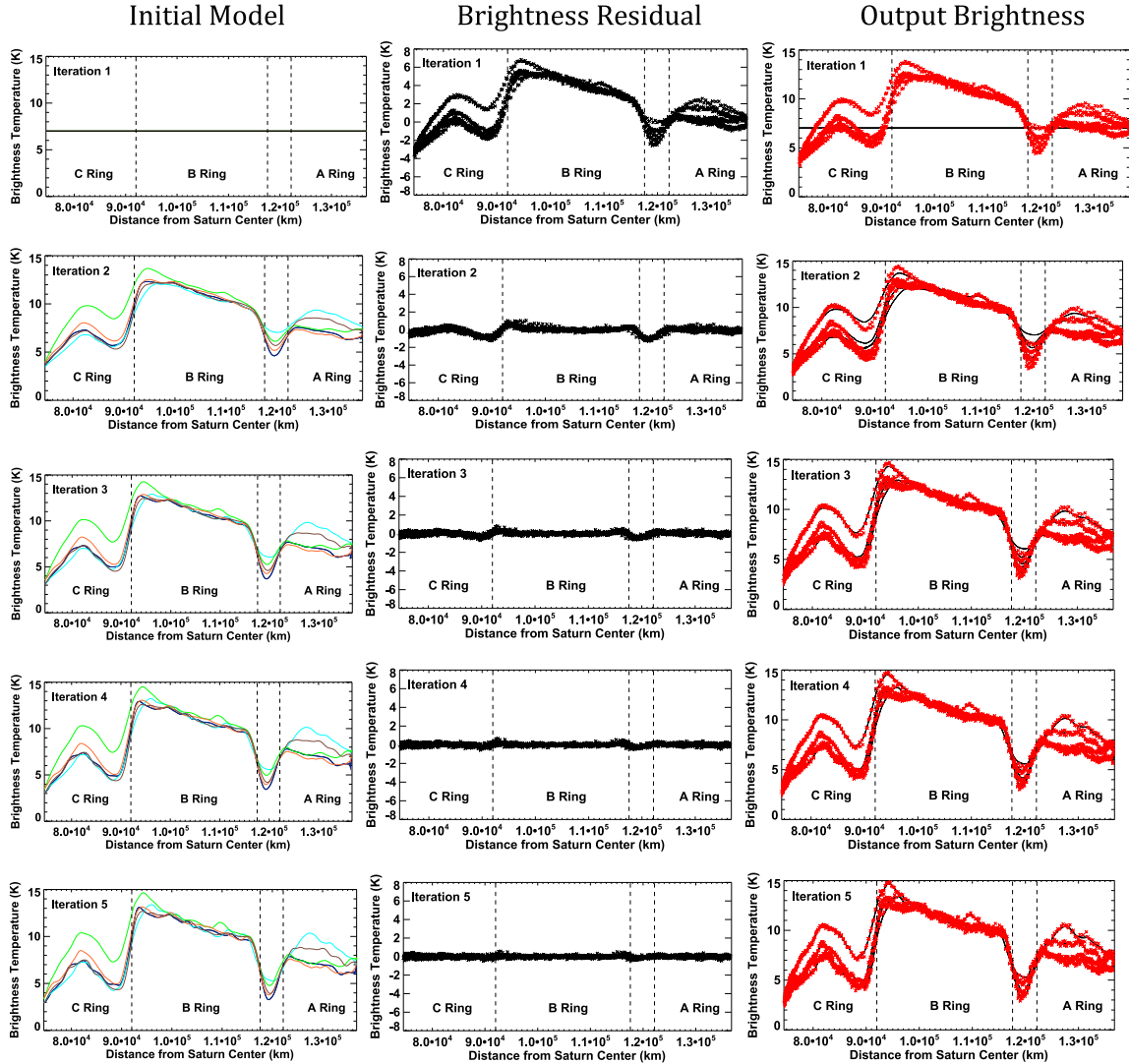


**Fig. 3.** Iterative process when applying deconvolution to a set of high-resolution observations (Rev028\_HIGH Polarization 2). Each row represents a single iteration. The left column shows the ring's brightness temperature reference model that we use to calculate sidelobe contributions in each iteration. We plot the brightness temperature vs. ring radius of the model at five representative azimuthal angles with different colors. Curves of different colors don't coincide with each other except in the B ring, which suggests a non-isotropic scattering profile in the C ring and asymmetric structure in the A ring. We will discuss this observed azimuthal variance further on in Sec. 2. The middle column shows the residual after subtracting modeled antenna temperature from observed antenna temperature, which represents the difference between scans of the reference ring model and the real ring brightness map. A RMS of  $\sim 0.2$  is reached after 5 iterations with no obvious structure being seen in the residual map at iteration 5. The right column shows the output of each iteration – the adjusted brightness temperature at each observation point (red crosses). The addition of the initial reference model (black curve) and the residual (shown in middle column) is used as the new reference model in the next iteration. (For interpretation of the references to colour in this figure legend, the reader is referred to the web version of this article.)

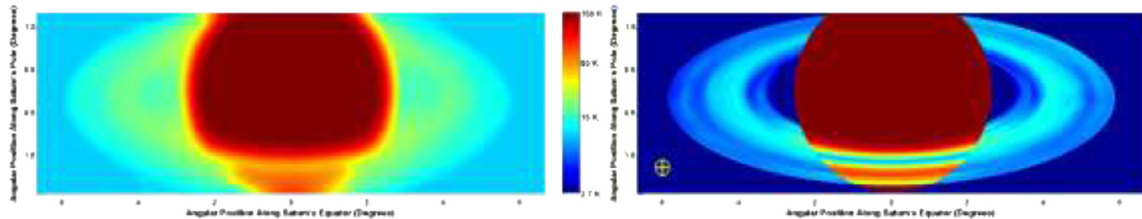


**Fig. 4.** Calibration of low-resolution Cassini Radar map scans obtained during Rev038\_2\_LOW (polarization 2) as projected onto the sky in degrees. Left panel: The collected antenna temperature map covers Saturn and its ring system using a combination of a large number of observations. Due to the wide antenna pattern and extensive sidelobe contribution from Saturn, the antenna temperature shows very little clear structure of the main rings. Right panel: The output brightness temperature map obtained through our calibration. Structures in the main rings are clearly visible with a RMS residual of  $\sim 2\%$ . The yellow circle in the lower left corner shows the main beam size, which is also the data resolution we can achieve after the calibration. (For interpretation of the references to colour in this figure legend, the reader is referred to the web version of this article.)

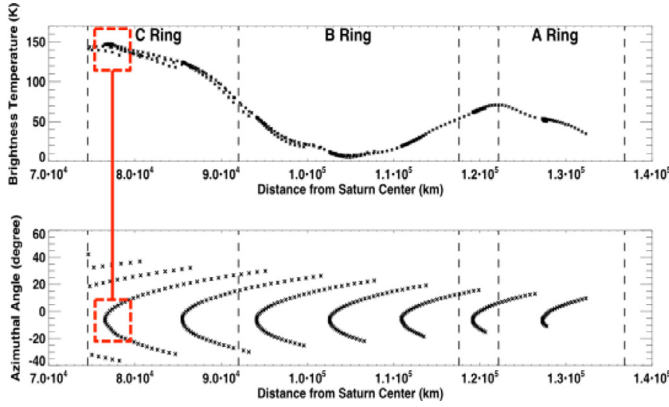


**Fig. 5.** Occultation observations in Rev038\_2\_LOW (Polarization 2); Upper panel: the radial brightness temperature profile of these occultation data (brightness temperature vs ring radius). We have combined observations at various azimuthal angles (as shown in the lower panel). Lower panel: the coverage of ring radius and azimuthal angles of the occultation observations shown in the upper panel. The small bumps in the red box in the upper panel correspond to the azimuth range in the red box in the lower panel, and appear to be  $\sim 1/10$  our radial resolution (our radial resolution is  $\sim 8000$  km). However these small bumps, which were collected at azimuthal angles approaching zero, are not radially resolved structure, but are actually caused by the phase function increase with decreasing scatter angle near zero azimuth.

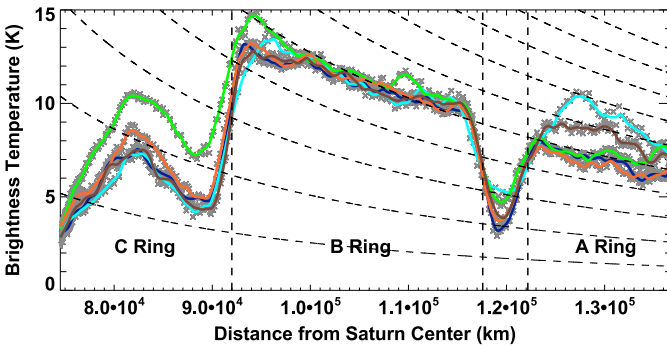


**Fig. 6.** Brightness temperature  $T_b$  versus ring radius (from Rev028\_HIGH polarization 2). For Rev028\_HIGH, each polarization has spoke scans at five distinct azimuthal angles (see upper panel in Fig. 2). We plot the best reference rings brightness models (solid lines) and output brightness temperatures (grey crosses) for the last iteration of our calibration process. Solid lines of different color indicate spoke scans at different azimuthal angles (the colors correspond to the azimuthal angles in the upper panel in Fig. 2). The black dashed lines show the trend of incident Saturn radiation, which decreases as one moves further away from Saturn's center. The bold vertical dashed lines indicate the borders between the different ring regions. (For interpretation of the references to colour in this figure legend, the reader is referred to the web version of this article.)

of the non-icy material (see Sec. 3.3), the absorptivity of water ice is thus 3 orders of magnitude smaller than the non-icy material. According to Kirchhoff's law, emissivity equals absorptivity, therefore the rings' intrinsic thermal emission, which is proportional to the effective emissivity of the ring particles, is dominated by the non-icy material contribution.

### 3.1. Radiation sources: Saturn emission and cosmic microwave background

As seen from a point in Saturn's rings, CMB radiation would come in isotropically from all directions at a temperature of 2.7 K, if Saturn were not there. The incident CMB radiation can be transmitted, scattered or absorbed by the rings, but due to the low emissivity of the rings' icy particles, the fraction of the CMB radiation absorbed by the C ring can be ignored. As we find as a result of this work, even in the middle C ring, where the intrinsic thermal emission is highest, the absorption rate is only about

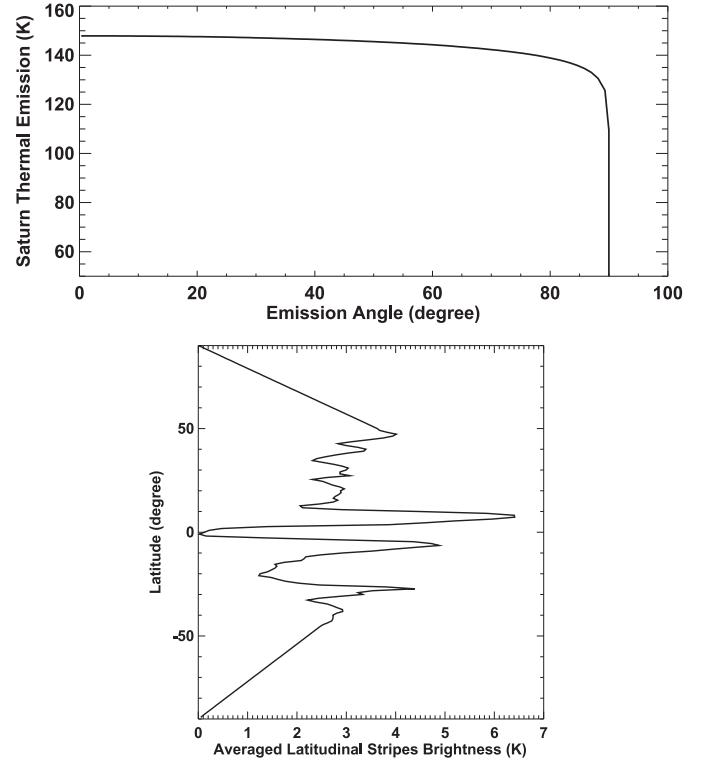


**Fig. 7.** Saturn radiation model from results of previous RADAR observations (Janssen et al. 2013). Upper panel: Limb darkened Saturn disk with brightness values as a function of emission angle. Lower panel: latitude-dependent stripes, brightness temperature variations versus latitude on top of the limb darkened disk.

6%, which will result in an absorption of  $\sim 0.16$  K from the CMB brightness. Considering the isotropic nature of the incident CMB, no matter in which direction one observes from the rings, one will always receive a CMB contribution of about 2.7 K. However, Saturn blocks out  $\sim 4\text{--}10\%$  of the sky as seen from the rings and, with it, also the CMB radiation from those directions. For objects as opaque and absorbing as Saturn, no CMB radiation can be transmitted through or reflected back, and in those directions where the sky is blocked by Saturn, the rings will receive Saturn radiation instead. In order to calculate the CMB contribution to the observed ring brightness, we will need to simulate how it is scattered by the rings, integrating the incident CMB radiation over  $4\pi$  steradians but omitting the portion blocked by Saturn. To limit computational complexity, we approximate the CMB contribution by removing 2.7 K from the Saturn thermal radiation and then combining the reduced Saturn radiation with fully isotropic CMB radiation. This leaves us with isotropic radiation of 2.7 K coming in from all directions, which will result in a  $\sim 2.7$  K contribution to the observed brightness temperature. We therefore use an effective Saturn thermal radiation which is 2.7 K less than the true Saturn thermal radiation to calculate the directly transmitted and scattered component in our Monte-Carlo code. In the end, the total simulated brightness temperature is the sum of directly transmitted effective Saturn radiation, scattered effective Saturn radiation, intrinsic thermal emission from the rings, and the 2.7 K CMB contribution.

Finally, due to Saturn's large solid angle as seen from the rings, a resolved Saturn thermal emission model is required. In this work, we use the Saturn radiation model derived from previous RADAR observations by Janssen et al. (2013). The model is presented as a limb-darkened disk with brightness temperature as a function of emission angle (see Fig. 7, panel 1), and with latitude-dependent stripes (see Fig. 7 panel 2) on top of the limb darkened disk. Since

these stripes have been longitudinally averaged, any longitudinal brightness variations are not captured by our model. In Janssen et al. (2013), the latitudinal stripes are derived independently from five observations. These variations are mainly concentrated at the equatorial region, and can be up to  $\sim 10$  K, which can cause noticeable uncertainties in the direct transmitted and forward scattered light when the observed rings are occulting Saturn. Fig. 7 panel 2 shows the averaged stripes among those five observations, which is what we applied in this work.

### 3.2. Optical depth

An important parameter in our model is the optical depth  $\tau$ , which is a measure of the particle column density, and therefore determines how much incident light is directly transmitted through the rings without interacting with any particles, how many times the incident light gets scattered by the ring particles before getting out of the ring layer, and also how much intrinsic thermal emission is generated within ring particles. We employ the normal optical depth profile measured by the Cassini Radio Science Subsystem (RSS) at  $\lambda_0 = 3.557$  cm (PDS Rings Node, Cuzzi et al., 2009). This profile was observed during the Rev 7 ingress ring occultation in 2005, at ring opening angle  $B = -23.6^\circ$ . We then convert  $\tau$  to the value at our wavelength,  $\lambda = 2.2$  cm. The ratio of the optical depth at these two wavelengths is obtained by integrating the ring particles' extinction cross-section calculated through Mie scattering theory.

At wavelength  $\lambda_0$  and  $\lambda$ , the optical depths of the ring slab are:

$$\begin{aligned} \tau_0(\lambda_0) &= \int_{a_{\min}}^{a_{\max}} Q_{\text{ext}}(a, \lambda_0) \cdot \pi a^2 \cdot n(a) da = n_0 \int_{a_{\min}}^{a_{\max}} Q_{\text{ext}}(a, \lambda_0) \cdot \\ &\quad \pi a^{2-q} \cdot da = n_0 \cdot C_0, \quad \lambda_0 = 3.557 \text{ cm} \\ \tau(\lambda) &= \int_{a_{\min}}^{a_{\max}} Q_{\text{ext}}(a, \lambda) \cdot \pi a^2 \cdot n(a) da = n_0 \int_{a_{\min}}^{a_{\max}} Q_{\text{ext}}(a, \lambda) \cdot \pi a^{2-q} \cdot \\ &\quad da = n_0 \cdot C, \quad \lambda = 2.2 \text{ cm} \\ \tau(\lambda) &= \left( \frac{C}{C_0} \right) \cdot \tau_0(\lambda_0). \end{aligned} \quad (11)$$

where  $Q_{\text{ext}}(a, \lambda)$  is the extinction coefficient for particles of size  $a$  at wavelength  $\lambda$  calculated from Mie scattering theory, and  $n(a)$  is the areal number density of particles with size  $a$ . The ring particles are assumed to have a power law size distribution  $n(a) = n_0 a^{-q}$ , where  $n_0$  is a constant. We calculate the parameter  $C_0$  at  $\lambda_0 = 3.557$  cm, and  $C$  at  $\lambda = 2.2$  cm in order to convert optical depth  $\tau_0(\lambda_0)$  at  $\lambda_0 = 3.557$  cm to  $\tau(\lambda)$  at  $\lambda = 2.2$  cm. For particle size parameters, we use the nominal values of  $a_{\min}$ ,  $a_{\max}$ , and  $q$  for the C, B and A ring particles as described in Sec. 3.3.

It is important to point out that, because of unresolved gaps caused by the wake structures in the B and A rings, the inferred apparent normal optical depth depends on the viewing angle of the original scan, with lower original viewing angle leading to a smaller normal optical depth value (Colwell et al., 2007; Colwell et al., 2010). The viewing angle is defined as the absolute value of the angle between the line-of-sight and the ring plane. The RSS optical depth profile we used here was collected at a viewing angle  $23.6^\circ$ , which is close to the viewing angle  $\sim 20^\circ$  of our radiometry data, and this represents the largest value of viewing angle scan we have from the RSS occultation. In this work, we are focused on analyzing the C ring observations, and this normal optical depth variation with viewing angle is negligible in the C Ring. We note that even though when looking at the outer C ring, where part of our beam may fall on the inner B ring, the change in normal optical depth beyond  $20^\circ$  viewing angle is not significant in the inner

B ring (Colwell et al., 2007). For the same reason, the azimuthal dependence of the line-of-sight optical depth in the A and B rings, where self-gravity wakes are present, is also not considered in our modeling efforts in this work.

Constrained by the resolution of Cassini Radar, what we obtain after the de-convolution process is a main-beam averaged brightness temperature. Considering that the main beam can cover a length-scale of 8000 km by 24,000 km on the ring plane (in low-resolution map scans), the particle properties (i.e., particle sizes, particle composition) and overall ring properties (i.e. occulting Saturn or not, optical depth) within the main beam can vary significantly. Part of the main beam may also fall on different objects (i.e., cold sky or Saturn's disk). The most accurate way to simulate the observed brightness temperature is to separate the main beam into smaller pieces within which the observed object properties do not change (i.e. ring particle sizes, compositions and local optical depth), simulate the brightness contribution from each small piece, and then convolve them with the main beam pattern. However, due to the large radial variation in optical depth, the number of computations required for each constant- $\tau$ -piece would be prohibitive. An alternative approximation is to subdivide the source observed within a given footprint into regions with similar ring particle properties (i.e., ring particle sizes and compositions) but with variable  $\tau$ , and then finding an average optical depth in each region. A special case is when part of the beam falls on occulting rings, while other parts fall on non-occulting rings, which we call transition data. For each ring annulus we have few transition data which do not cover enough azimuthal angles near the boundary between occulting and non-occulting regions. These transitions are very sharp, especially in the C ring. Thus it becomes very difficult to retrieve the full shape at these transition regions, which results in larger errors in the transition data. Therefore, in the following analysis, we do not use these transition data.

Specifically, for each C ring occultation observation, we separate the source observed within a footprint into three regions depending on which properties are relevant: occulting C&D ring (OC&D), occulting B ring (OB) and the Saturn disk. For each C ring non-occultation observation, we separate the source into two regions: non-occulting C&D ring (NOC&D) and non-occulting B ring (NOB). At the inner edge of the C ring, the main beam may lie partially in the D ring. Since the D ring has very low optical depth and contributes little to the brightness, we assume that D ring particles are similar to C ring particles and combine them together denoted as C&D. For each of the NOC&D, NOB, OC&D and OB regions, we calculate the effective optical depth. When light with intensity  $I$  is incident upon a ring plane with normal optical depth  $\tau$  at incidence angle  $\beta$ , the light that is transmitted is proportional to  $e^{-\tau/\cos\beta}$ , and thus the light scattered by the ring particles is proportional to  $(1-e^{-\tau/\cos\beta})$ . Therefore, we calculate the effective optical depth for each ring region within a footprint by averaging the optical depth with the gain pattern as:

$$\begin{aligned} &\left( 1 - e^{-\tau_{\text{eff}}^i / \mu_{\text{eff}}} \right) \\ &= \frac{\iint_{\text{mainbeam on } i} \left( 1 - e^{-\tau(\theta, \phi) / \mu(\theta, \phi)} \right) G(\theta, \phi) \sin\theta d\theta d\phi}{\iint_{\text{mainbeam on } i} G(\theta, \phi) \sin\theta d\theta d\phi}. \end{aligned} \quad (12a)$$

and the fraction of the main beam area filled by each of the regions is:

$$f_i = \frac{\iint_{\text{mainbeam on } i} G(\theta, \phi) \sin\theta d\theta d\phi}{\iint_{\text{full mainbeam}} G(\theta, \phi) \sin\theta d\theta d\phi}. \quad (12b)$$

where  $i = (\text{OC&D}, \text{OB}, \text{NOC&D}, \text{NOB})$ .  $\tau_{\text{eff}}^i$  is the effective normal optical depth for each part  $i$  that falls on the rings,  $f_i$  is its fractional contribution to the total brightness,  $\mu_{\text{eff}}$  is the cosine of the incidence angle at beam center,  $(\theta, \phi)$  is the angular deviation from

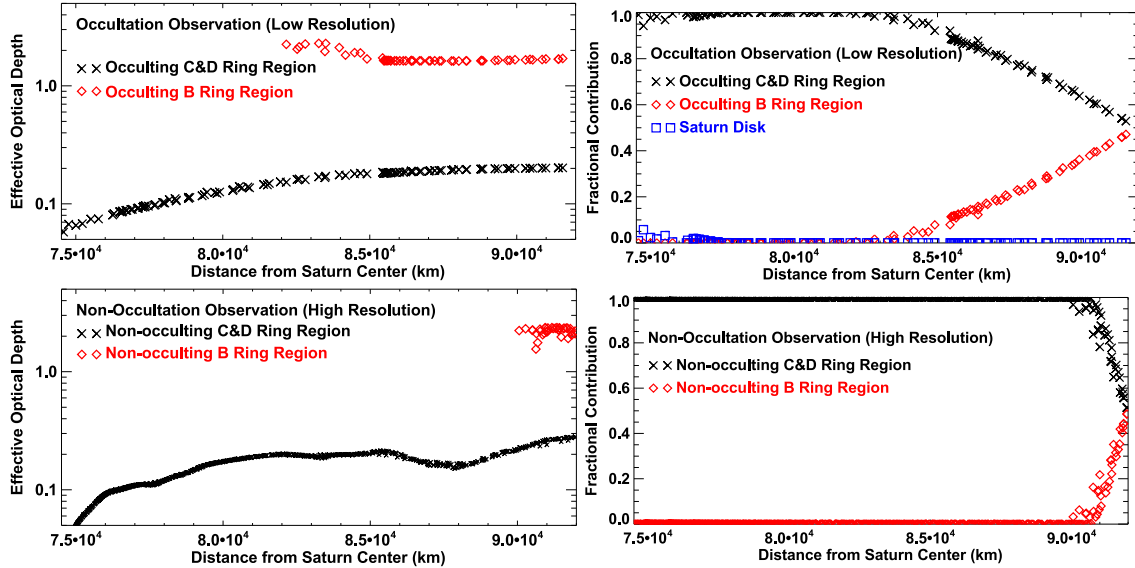


**Fig. 8.** Upper Panels: Occultation observation in Rev038\_2\_LOW on the C Ring. Radially varying effective optical depth  $\tau_{\text{eff}}^i$ ,  $i = (\text{OC\&D}, \text{OB})$  (see Eq. 12a) (left panel) and corresponding fractional contribution to the main beam brightness  $f_i$ ,  $i = (\text{OC\&D}, \text{OB})$  (see Eq. 12b) (right panel) from occulting C&D rings (black crosses) and occulting B ring (red diamonds). We also plot the fractional contribution directly from Saturn's disk (blue squares in right panel). Lower Panels: Non-occultation observation in Rev028\_HIGH on the C Ring: Radially varied effective optical depth  $\tau_{\text{eff}}^i$ ,  $i = (\text{NOC\&D}, \text{NOB})$  (left panel) and corresponding fractional contribution to the main beam brightness  $f_i$ ,  $i = (\text{NOC\&D}, \text{NOB})$  (right panel) from non-occulting C&D rings (black crosses) and non-occulting B ring (red diamonds). (For interpretation of the references to colour in this figure legend, the reader is referred to the web version of this article.)

the main beam center, and  $G$  is the radiometer main beam gain pattern defined in Sec. 2. At each angular direction  $(\theta, \phi)$ , we determine the corresponding local optical depth  $\tau(\theta, \phi)$  using the radially dependent optical depth profile as described in Eq. (11). In addition to these contributions, we also have  $f_{\text{Saturn}}$  which is the fraction of the main beam that falls directly on Saturn's disk. Taking into account the CMB radiation issue we discussed in Sec. 3.1, we simulated the brightness contribution from each of these parts with the effective optical depth and an effective Saturn thermal emission that is 2.7 K lower than the true radiation value. In the end, the simulated brightness temperature of each observation point for the occultation observations is:

$$\begin{aligned} T_{\text{occ\_simulate}} = & (T_{\text{direct\_OC\&D}} + T_{\text{scatter\_OC\&D}} + T_{\text{thermal\_OC\&D}}) \cdot f_{\text{OC\&D}} \\ & + (T_{\text{direct\_OB}} + T_{\text{scatter\_OB}} + T_{\text{thermal\_OB}}) \cdot f_{\text{OB}} \\ & + (T_{\text{Saturn\_radiation}} - 2.7\text{K}) \cdot f_{\text{Saturn}} \\ & + 2.7\text{K}. \end{aligned} \quad (13a)$$

and for the non-occultation observations:

$$\begin{aligned} T_{\text{Non-occ\_simulate}} = & (T_{\text{scatter\_NOC\&D}} + T_{\text{thermal\_NOC\&D}}) \cdot f_{\text{NOC\&D}} \\ & + (T_{\text{scatter\_NOB}} + T_{\text{thermal\_NOB}}) \cdot f_{\text{NOB}} \\ & + 2.7\text{K}. \end{aligned} \quad (13b)$$

where  $T_{\text{direct}_i}$ ,  $i = (\text{OC\&D}, \text{OB})$  are the directly transmitted effective Saturn thermal emission;  $T_{\text{scatter}_i}$ ,  $i = (\text{OC\&D}, \text{OB}, \text{NOC\&D}, \text{NOB})$  are the scattered effective Saturn thermal emission; and  $T_{\text{thermal}_i}$ ,  $i = (\text{OC\&D}, \text{OB}, \text{NOC\&D}, \text{NOB})$  are the intrinsic thermal emission from the rings particles all simulated by SimRings.

In Fig. 8, we investigate the radially varied effective normal optical depth  $\tau_{\text{eff}}^i$  (see Eq. 12a) for different parts of the rings and their fractional contribution  $f_i$  (see Eq. 12b) to the averaged brightness in the main beam, for a set of typical occultation observations of the C ring in low-resolution (Rev038\_2\_LOW, upper panels) and non-occultation observations in high-resolution (Rev028\_HIGH, lower panels). The low-resolution observation has a resolution of  $\sim 8000$  km and the main beam begins falling partially on the B ring beyond  $\sim 82,000$  km. Lower panels show a high-resolution of  $\sim 2000$  km, and only observations centered in

the outer C ring beyond 90,000 km contain contributions from the B ring.

### 3.3. Ring particle composition and size distribution

The ring particle composition is used to determine the material's effective dielectric constant based on the Maxwell-Garnett mixing rule of Effective Medium Theory (EMT; see, Bohren and Huffman, 1983). We assume the ring particles are made of porous water ice with non-icy material embedded in the form of small inclusions. Assuming the inclusions are spherical, the complex effective dielectric constant of a porous mixture of water ice and intermixed non-icy material can be expressed as

$$\varepsilon_{\text{eff}} = \varepsilon_{\text{ice}} \left[ 1 + \frac{3(f_v(1-f_p)\frac{\varepsilon_{\text{non-ice}}-\varepsilon_{\text{ice}}}{\varepsilon_{\text{non-ice}}+2\varepsilon_{\text{ice}}} + f_p\frac{1-\varepsilon_{\text{ice}}}{1+2\varepsilon_{\text{ice}}})}{1 - (f_v(1-f_p)\frac{\varepsilon_{\text{non-ice}}-\varepsilon_{\text{ice}}}{\varepsilon_{\text{non-ice}}+2\varepsilon_{\text{ice}}} + f_p\frac{1-\varepsilon_{\text{ice}}}{1+2\varepsilon_{\text{ice}}})} \right], \quad (14)$$

where  $\varepsilon_{\text{non-ice}}$  and  $\varepsilon_{\text{ice}}$  are the complex dielectric constants of the non-icy mixture and pure ice, respectively,  $f_p$  is the particle porosity and  $f_v$  is the volume fraction of non-icy material mixed within the ice. In the limit that  $f_v \rightarrow 0$ , Eq. (14) simply describes the dielectric constant of a porous ice particle, whereas in the limit  $f_p \rightarrow 0$ , Eq. (14) reduces to the more general formula for a single component embedded in an ice medium (e.g., Bohren and Huffman, 1983; Cuzzi et al., 2014). We primarily use silicates as the candidate for the intermixed non-icy material (see Sec. 5.4) which has dielectric constant  $\varepsilon_{\text{silicate}} = 5.38 - i \cdot 0.134$  (Cuzzi et al., 1980).

As for the dielectric constant of water ice, we follow the relations used by Grossman (1990) and Dunn et al. (2002). The complex index of refraction is  $n = n_r - i n_i$ . The real part of the refractive index,  $n_r$ , is 1.78, while the imaginary part of the refractive index is  $n_i = \alpha_\lambda \lambda / 4\pi$ , where  $\alpha_\lambda$  is the absorption coefficient. Mishima et al. (1983) provided the laboratory results for absorption coefficient

$$\alpha_{H_2O_{\text{ice}}} = \frac{A_0}{T} \frac{e^{hcv_0/kT}}{(e^{hcv_0/kT} - 1)^2} \left( \frac{v}{v_0} \right)^2 + B_0 v^4. \quad (15)$$

where  $v$  is wavenumber in  $\text{cm}^{-1}$ ,  $v_0 = 233\text{cm}^{-1}$ ,  $A_0 = (1.188 \pm 0.01) \times 10^5 \text{cm}^{-1}\text{K}$ , and  $B_0 = (1.11 \pm 0.03) \times 10^{-6} \text{cm}^3$ .

Using the relation between refractive index and dielectric constant  $\varepsilon = n^2$ , the water ice dielectric constant at the C ring's physical temperature of  $T_{\text{ring}} = 85 \text{ K}$  (Hanel et al. 1981; 1982) and a wavelength of  $\lambda = 2.2 \text{ cm}$  is  $\varepsilon_{\text{ice}} = 3.17 - i \cdot 6.68 \times 10^{-5}$ . As a comparison, the water ice dielectric constant used in Cuzzi et al. (1980) for C ring particles at  $T_{\text{ring}} = 100 \text{ K}$  and  $\lambda = 2.2 \text{ cm}$  is  $\varepsilon_{\text{ice}} = 3.17 - i \cdot 1.2 \times 10^{-4}$ , while the calculated value at corresponding  $T_{\text{ring}}$  and  $\lambda$  with the relations we use is  $\varepsilon_{\text{ice}} = 3.17 - i \cdot 1.1 \times 10^{-4}$ .

For the ring particles, we employ a power law size distribution as described in Sec. 3.2,  $n(a) = n_0 a^{-q}$ , where  $n_0$  is a constant. The particle size distribution parameters determined from the Voyager radio occultation observations give a power law index  $q = 3.11$ , and a maximum particle size  $a_{\text{max}} = 4.5 \text{ m}$  for the inner and middle C ring region ( $74,430 - 84,460 \text{ km}$ ), and  $q = 3.05$ , and a maximum particle size  $a_{\text{max}} = 2.4 - 5.3 \text{ m}$  for the C ring ramp ( $90,640 - 91,970 \text{ km}$ ), assuming a thin-layered ring model (Zebker et al., 1985). Furthermore, the C ring shows a minimum particle size of  $0.4 \text{ cm}$  from the stellar occultation observations (Harbison et al., 2013). The differential optical depth values from the Cassini RSS occultation also supports the  $0.4 \text{ cm}$  minimum size, but with a steeper size distribution slope of  $q = 3.2$  or slightly larger (Cuzzi et al., 2009; Marouf et al., 2008). In this work, we choose as our nominal values  $a_{\text{min}} = 0.4 \text{ cm}$ ,  $a_{\text{max}} = 450 \text{ cm}$ , and  $q = 3.15$  for the C and D ring particles. On the other hand, A and B ring particles show a similar rather flat distribution with  $q = 2.75$ , minimum size  $a_{\text{min}} = 30 \text{ cm}$ , and maximum size  $a_{\text{max}} = 20 \text{ m}$  derived from the Earth-based 28 Sgr occultation (French and Nicholson, 2000). This maximum size is a factor of two larger than the Voyager RSS result for the A ring particles, where  $a_{\text{max}} = 5 - 11 \text{ m}$  (Zebker et al., 1985). Here, for all B ring regions we choose  $a_{\text{min}} = 30 \text{ cm}$ ,  $a_{\text{max}} = 630 \text{ cm}$ , and  $q = 2.75$ . We note that the determination of all these A/B ring particle size distributions ignore the gravitational wake structures. In this work, we focus on the C ring observations, which is not very sensitive to the choice of the A/B ring particle size distribution parameters.

#### 3.4. Scattering phase function

For the scattering and extinction cross-sections of individual ring particles, which vary with particle size and dielectric constant, we use Mie theory. When the ring particle size parameter  $x$ , which is the ratio of particle circumference to wavelength, is less than an upper bound of  $x \sim 5$  (Cuzzi and Pollack, 1978), a Mie phase function, which is derived from spherical particles, is adequate to describe each single scattering, even for non-spherical particles. In Saturn's C ring, millimeter - centimeter scale particles are dominant in the scattering process and the size parameters of most small particles are less than the upper bound at a wavelength of  $2.2 \text{ cm}$ . Therefore a Mie phase function is a good approximation in most regions in the C ring. However, as the ring particle size and number density (optical depth) grow in the B ring, two factors, the non-sphericity and close packing of ring particles, cause the phase function to deviate from simple Mie scattering. To that end, where Mie scattering alone is inadequate, we introduce a phase function that is a linear combination of Mie and isotropic scattering phase functions (Dunn et al., 2002)

$$P(\theta) = (1 - f_{\text{iso}}) \cdot P_{\text{mie}}(\theta) + f_{\text{iso}} \cdot \frac{1}{4\pi} \quad (16)$$

where  $f_{\text{iso}}$  is the fraction of isotropic scattering. According to previous VLA observations at a wavelength of  $2.0 \text{ cm}$ , the combination of Mie and isotropic phase functions works well for the B ring, while a pure Mie phase function works best for the C ring (Dunn et al., 2002). We consider  $f_{\text{iso}}$  for the B ring particles as a variable to be determined in our analysis.

## 4. Results

For a particle size distribution with our nominal choice of power law index  $q = 3.15$ , small particles dominate the scattering process in the C ring. Most of these small particles have a size parameter smaller than the bound beyond which non-sphericity becomes important. Furthermore, considering that the C ring particles are relatively widely separated due to the low optical depth there, they can be treated as independent spheres. Therefore, Mie scattering theory is expected to be a good approximation for the scattering process in the C ring. In this section, we compare the simulated brightness temperature with the observations in order to determine the C ring particle composition in terms of porosity and non-icy material fraction.

#### 4.1. Occultation region at small Azimuths: ring particle porosity

We first analyzed the occulted region of Saturn on the C ring in low-resolution map scans. These brightness data are composed of directly transmitted radiation, scattered Saturn radiation, and intrinsic thermal emission. However, the directly transmitted and forward-scattered sources of Saturn radiation are an order of magnitude larger than the intrinsic thermal emission. Therefore, in these occultation observations the brightness temperature is not very sensitive to the non-icy material fraction, providing us with an opportunity to investigate ring particle porosity alone. As shown in the output brightness temperature profile of Rev028\_HIGH (Fig. 6), most parts of the C ring are no brighter than  $10 \text{ K}$  at larger azimuthal angles. The non-occultation brightnesses are composed of scattered Saturn radiation and intrinsic thermal emission. In these cases, even if the intrinsic thermal emission contributes half of the brightness, it is still no larger than  $5 \text{ K}$ . Moreover, the intrinsic thermal emission is originally emitted by the ring particles isotropically and thus its value shouldn't depend in a significant way on the azimuthal angle of the observing point. That is to say, the intrinsic thermal emission at smaller azimuthal angles should also be no larger than  $5 \text{ K}$ , which is an order of magnitude smaller than the directly transmitted and forward-scattered Saturn radiation in the occultation data.

The data were collected during Rev028\_LOW, Rev038\_1\_LOW, Rev038\_2\_LOW and Rev039\_LOW, when the rings had opening angle  $B = \sim 20^\circ$ . Considering that our main beam can cover a  $\sim 8000 \text{ km}$  to  $24,000 \text{ km}$  region, when observing radial locations outside  $82,000 \text{ km}$  the averaged brightness in the main beam contains contributions from the inner B ring (see Fig. 8). Therefore, in order to simulate the brightness temperature in these observations, the scattering properties of the inner B ring particles are also required. As opposed to the C ring particles, non-sphericity and close packing effects become important for the B ring particles and a modified phase function such as the one given in Eq. (16) is required. We determine the value of  $f_{\text{iso}}$  by matching the data in the outer C ring. Initially, we assumed non-porous ring particles with our nominal size distributions throughout the whole of the C and B rings, respectively (see Sec. 3.3), and specifically for the B ring a value of  $f_{\text{iso}} = 0$ . However, we found that the modeled brightness temperature is much smaller than observed (see Fig. 9 with, e.g., data from Rev038\_1\_LOW). Notice that the observations show significant scatter, because at each ring radius data are collected at various azimuthal angles (see Fig. 5, lower panel). In the C ring, half of the brightness in "occultation" geometries is contributed by scattered Saturn radiation and the scattering phase function varies quickly at these small azimuthal angles.

The directly-transmitted Saturn radiation is fixed since the optical depth is fixed. Therefore, this mismatch indicates that we need a more forward-directed scattering phase function for the C ring particles. We can improve the fit of the phase function either by

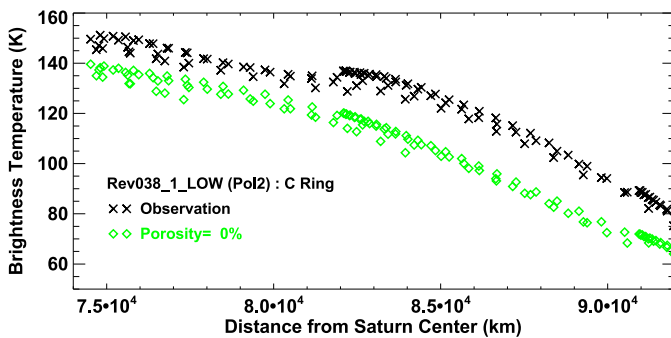


**Fig. 9.** Brightness temperature vs. ring radius plot of occultation observations in the C ring during Rev038\_1\_LOW (polarization 2). Black crosses: observed brightness temperature. Green diamonds: simulated brightness temperature assuming zero porosity.

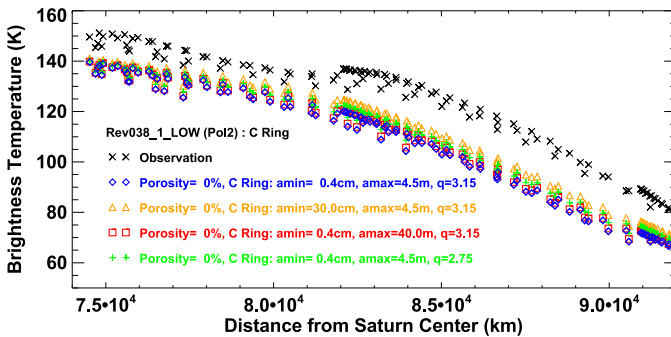


**Fig. 10.** Brightness temperature vs. ring radius for occultation observations of the C ring during Rev038\_1\_LOW (polarization 2). The black crosses are the observed brightness temperature, while the blue diamonds are the simulated brightness temperature assuming zero porosity and the nominal C ring particle size distribution  $a_{\min} = 0.4 \text{ cm}$ ,  $a_{\max} = 450 \text{ cm}$ ,  $q = 3.15$ . Orange triangles: An increase of  $a_{\min}$  from 0.4 cm to 30 cm. Red squares: An increase of  $a_{\max}$  from 4.5 m to 40 m. Green plus signs: A decrease of  $q$  from 3.15 to 2.75. (For interpretation of the references to colour in this figure legend, the reader is referred to the web version of this article.)

increasing the average C ring particle size, as large particles are strong forward-scatterers, or decreasing the real component of the dielectric constant, for example, by making the whole particle uniformly more porous, or assuming a core-mantle ring particle structure with a solid core and porous mantle. Due to the complication of the core-mantle ring particle structure in our simulation, we defer treatment of the core-mantle particles to Section 5.2. We will show there that by selecting appropriate parameters for the core-mantle model, its phase function can be made to closely match that of the intramixed model, and thus will not change the simulated scatter component for the occultation and non-occultation data.

We first attempted to increase the number of larger particles in the C ring by altering the parameters in the particle size distribution by either increasing the minimum size  $a_{\min}$ , maximum size  $a_{\max}$  or decreasing the power law index  $q$ . We note that the parameters in the power law size distribution have been fairly well constrained by previous work, with a much smaller range than what we test here (Marouf et al., 2008). However, we found that even for choices of the parameters at the extremes of what we consider a reasonable range, the simulated brightness temperature is still much lower than observed (see Fig. 10, specifically Rev038\_1\_LOW, polarization2 as an example). We also included an additional thermal emission contribution due to non-icy material, which can at most be about 5 K, but again found that the total simulated brightness is still not high enough to match the observations.

Second, we chose to model the ring particles as porous. Because the outer C ring brightness temperature has a large contribution from the inner B ring, the porosity of the C ring and B ring particles,  $f_{p\_CRing}$  and  $f_{p\_BRing}$  need to be determined at the same time. For the C ring porosity, we vary  $f_{p\_CRing}$  from 0% to 90%, in steps of 5%. At this stage, we are not able to determine the B ring particle porosity independently from the C ring observations. In fact, as the scattering phase function for the B ring particles is a combination of Mie and isotropic functions, and porosity only affects the Mie phase function piece, the B ring particle scattering phase function is much less sensitive to porosity than compared to the C ring. Moreover, previous work has suggested that A ring particles could be as much as 55% porous (Porco et al., 2008; see, also Morishima et al., 2016), thus it is reasonable to assume that the B ring particle porosity may lie somewhere in between the A ring and C ring values. Recent work also suggests high porosity of the B ring particles based on its seasonal temperature variation (Reffet et al. 2015). We considered two cases: (1)  $f_{p\_BRing} = f_{p\_CRing}$ ; and (2)  $f_{p\_BRing} = f_{p\_ARing} = 55\%$ . We combine the occultation data in all four low-resolution map scan occasions and find that our best fit model is obtained when C ring particles are 75% porous in both cases, with a RMS  $\sim 3.8 \text{ K}$ , about 2–5% of the observed brightness. By adding 75% porosity to the ring particles, the real part of the effective dielectric constant becomes  $\sim 1.45$ . At the outer C ring, where the main-beam brightness starts to contain contributions from the inner B ring, we assume that B ring particles scatter with a phase function  $P(\theta) = (1 - f_{iso\_BRing})P_{mie}(\theta) + f_{iso\_BRing}/4\pi$ . We vary  $f_{iso\_BRing}$  from 0% to 100%, in increments of 10%, and find that a value of  $f_{iso\_BRing} = 20\%$  provides the best fit to the outer C ring data. Fig. 11 shows how our best-fit parameters match the observations. The simulation results don't change much no matter what value for the B ring porosity is assumed and in Fig. 11 we only show the case when assuming  $f_{p\_BRing} = 55\%$ . The result confirms our earlier assumption that the brightness contribution from B ring particles is not very sensitive to their porosity, since the best-fit C ring porosity value remains the same as the B ring particles porosity varies between 55% and 75%.

In Fig. 12, we plot the single scattering phase function integrated over the C ring particle size distribution for all our attempts to match the high brightness in the occultation data (i.e., increasing the minimum particle size, maximum size, decreasing the power law index, and adding porosity), which shows how adding 75% porosity is able to increase the simulated brightness enough to match the observation while merely changing the particle size distribution parameters cannot. By adding 75% porosity, the bending angle of intrinsic refraction tends to be smaller and more light gets scattered into the forward direction. The light scattered into large scattering angles is suppressed, while the light scattered into angles smaller than  $\sim 30^\circ$  increases greatly. Since Saturn has a  $\sim 40\text{--}55^\circ$  angular radius as seen from the C ring, most incident Saturn radiation is scattered less than  $30^\circ$  before reaching the observer in occultation observations, and therefore their simulated brightness temperatures increase considerably by adding 75% porosity.

The average brightness temperature of these observations is in between  $\sim 80\text{--}150 \text{ K}$ . We find that the best fit RMS is about 2–5% of the average observed brightness temperature, which is comparable to our calibration error ( $\sim 2\%$ ). On the other hand, the portion of the Saturn disk blocked by the C ring lies between the latitudes of 5 to  $25^\circ$ s south, where a longitudinally-variable bright Saturn radiation band has been discovered (Janssen et al., 2013). The variation in longitude can be as large as  $\sim 10 \text{ K}$ , which can cause an increase in the C ring brightness temperature of  $\sim 6 \text{ K}$  even for the comparatively optically thick middle C ring with  $\tau \sim 0.2$ . This may be another factor that can cause errors in the fitting process.

Arecibo observations (Nicholson et al., 2005) have yielded a stringent upper limit of 3% on the back scattering cross-section

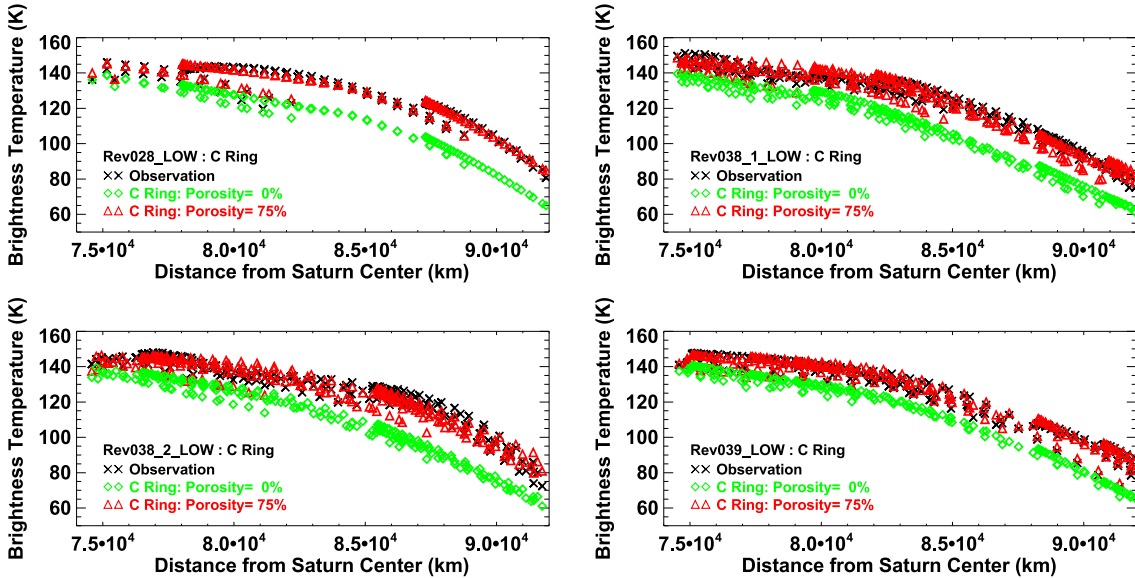


**Fig. 11.** Brightness temperature model as compared to actual observations for C ring particles with 75% porosity. Plotted is the brightness temperature vs. ring radius for occultation observations of the C ring during Rev028\_LOW (upper left), Rev038\_1\_LOW (upper right), Rev038\_2\_LOW (lower left) and Rev039\_LOW (lower right). For each occasion, we have combined data from all available polarizations. Black crosses: observed brightness temperature. Green diamonds: simulated brightness temperature assuming zero porosity. Red triangles: simulated brightness when assuming C ring particles are 75% porous. (For interpretation of the references to colour in this figure legend, the reader is referred to the web version of this article.)

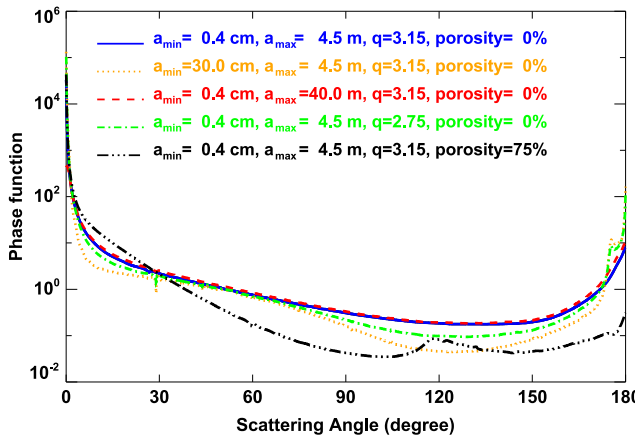


**Fig. 12.** Single scattering phase function integrated over the C ring particle size distribution for all our trial cases. Case 1 (blue): nominal particle size distribution; zero porosity. Case 2 (yellow): increase of the minimum size from 0.4 cm to 30 cm; zero porosity. Case 3 (red): increase of the maximum particle size from 4.5 m to 40 m; zero porosity. Case 4 (green): decrease of the distribution power law index from 3.15 to 2.75; zero porosity. Case 5 (black): nominal particle size distribution; 75% porosity. (For interpretation of the references to colour in this figure legend, the reader is referred to the web version of this article.)

of the C ring. With these highly porous ring particles, we simulated the back scattering from the C ring and obtained a very low, normalized backscatter cross-section of about 3%, consistent with the observations. Given that some of the smaller satellites in the Saturn system have bulk porosities in excess of 60% (Thomas et al., 2007; Johnson et al., 2005), and the recent works by the Rosetta team that reported a bulk porosity of 70 – 80% for comet 67P/Churyumov-Gerasimenko (Sierks et al., 2015; Kofman et al., 2015), it may not be surprising that individual ring particles can be so porous. Porco et al. (2008) also suggested that the A ring particles are very porous due to the low internal mass density. Recently, Morishima et al. (2016) have matched CIRS data within the A ring by assuming that A ring particles have cores with porous icy mantles with values for the porosity similar to what we find here

(see also, Sec. 5.1). The finding is interesting because although particle mean densities in the A ring are not expected to be so low due to the presence of self gravity wakes (e.g., see French et al., 2007), particles that have dense cores but, with fairly porous surface layers were found to best fit the data. This suggests that particles can be porous even under relatively vigorous collisional conditions. Given that there are no observed self gravity wakes in the C ring, it may not be unreasonable then to consider that particles may also be porous in the C ring.

One possible explanation might be that impact gardening due to micrometeoroid bombardment, which creates a regolith of increasing depth over time (e.g., Elliott and Esposito, 2011), may play a role in increasing particle porosity. Collisions among ring particles occur frequently within the C ring, but at relatively low (mm/s) velocities, when compared to impacts by extrinsic micron-sized meteoroids ( $\sim 10$  times more frequent for the nominal choice of flux, Sec. 5.1). However, secondary impacts that arise as a result of the ejected material from the primary micrometeoroid impact should occur much more frequently than inter-particle collisions and at velocities of up to tens of meters per second (see ballistic transport process as discussed in Cuzzi and Estrada, 1998). These secondary impacts might kick up loosely bound regolith particles such that a considerable “exchange” of material may happen *locally* between neighboring ring particles keeping their regoliths fluffy. Thus, even though inter-particle collisions may have a tendency to compact a ring particle surface, it might be possible that the ring particles can achieve a quasi-equilibrium porous regolith that results from a balance of these combined impact and collisional processes.

#### 4.2. High resolution scans at ring Ansa: ring particle non-icy material fraction

While occultation observations mainly reveal the strength of the forward directed part of the scattering phase function, non-occultation observations in high-resolution spoke scans depend more on the scattering phase function at larger scattering angles. By adding 75% porosity we have made the phase function more forward-directed to match the small angle scattering in the

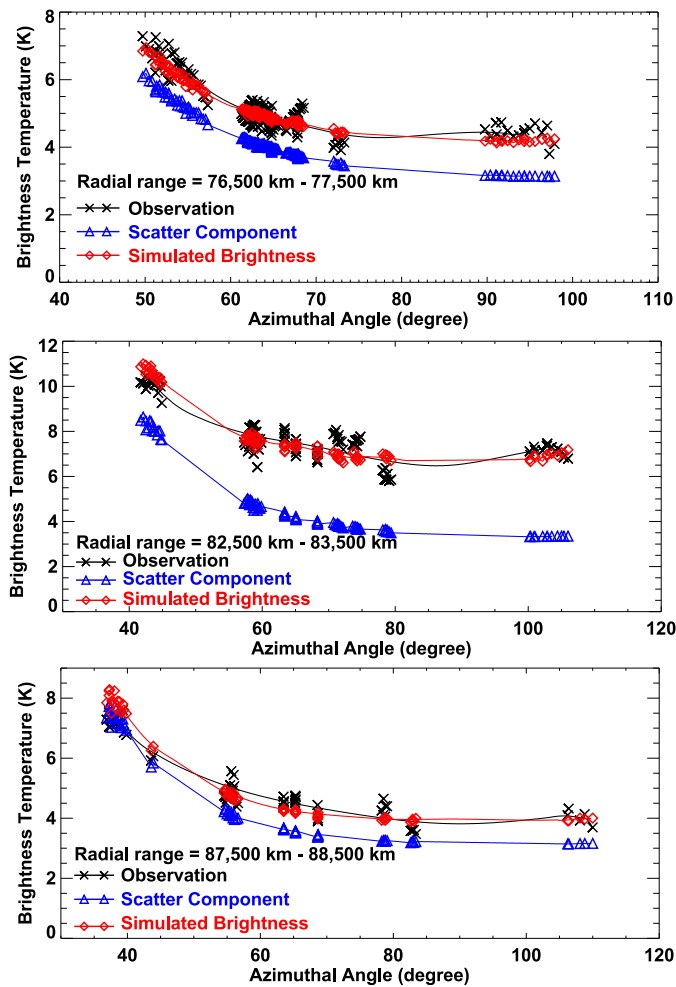


**Fig. 13.** Scattering profile: brightness temperature versus azimuthal angle curves at three different ring radii for the inner (76,500 km–77,500 km), middle (82,500 km–83,500 km) and outer C ring (87,500 km–88,500 km). The azimuthal angle is the angle between the projection of Cassini onto the ring plane and the observation point in Saturn-centered coordinates. All observation data come from Rev028\_HIGH. We plot the observed brightness temperature (black crosses), scattering component with CMB contribution (blue triangles) and simulated brightness temperature (red diamonds; addition of scatter component, CMB contribution and intrinsic thermal emission). We have added ~2%, ~6% and ~1.5% non-icy material in the ring annulus for panels 1, 2 and 3, respectively. The simulated brightness temperature matches the observations well. The observed brightness at some azimuthal angles are scattered due to the relatively large radial width of the ring annulus. In the middle C ring (panel 2), the polarization effect is most obvious between 60 to 80° azimuth. All the observations (black crosses) above the simulated brightness (red diamonds) are collected at polarization 2 and 3, while the ones below the simulated brightness are at polarization 1 (horizontal to the ring plane, see Sec. 2 for more details). This polarization variation in observed brightness will have the effect of increasing the uncertainty of our final non-icy material fraction profile. (For interpretation of the references to colour in this figure legend, the reader is referred to the web version of this article.)

occultation observations. We further investigated the scattering profile in high-resolution spoke-scan non-occultation observations to check how this phase function behaves at large scattering angle. Fig. 13 shows observations from three ring annuli in the inner, middle and outer C ring. The simulated scattering profile (brightness temperature vs azimuthal angle) matches the data fairly well. At the middle C ring, intrinsic thermal emission contributes almost half of the brightness, which indicates that there must be some non-icy material included in the ring particles.

We simulated the Saturn radiation scattered by porous ring particles with  $f_p = 75\%$  for non-occultation observations during Rev028\_HIGH. Given the non-icy fraction of each ring particle's

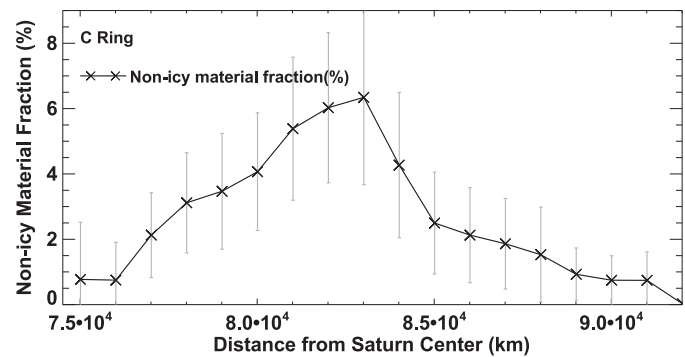


**Fig. 14.** The derived radial variation of non-icy fraction reaches its maximum of ~6.3% silicate by volume in the middle of the C ring and gradually decreases inward, and more sharply outward. The grey vertical lines show the range of one standard deviation.

composition, our Monte-Carlo code is able to simulate the magnitude of the thermal emission. The scattered component doesn't significantly change as we add non-icy material (i.e. silicate) to the ring particles. We therefore are able to determine the non-icy material fraction by adding non-icy material to the C ring particles until the simulated brightness, which is a combination of scattering component, thermal emission and CMB contribution, matches the observation. The results of this analysis justify the necessity for including intrinsic thermal emission in order to match the observed brightness temperature, especially around ~83,000 km in the middle C ring, where the brightness is observed to increase significantly beyond what can be attributed to scattered radiation from Saturn. We find that more than half of the brightness temperature comes from intrinsic thermal emission, while the shape of the profile is well-matched by scattered radiation (see Fig. 13, middle panel).

Microwave thermal emission is directly related to the abundance of non-icy material. For reasons that will become clear below (see Sec. 5, and specifically Sec. 5.4 for a brief discussion of other candidate materials), we find that the best candidate material for the non-icy component is silicate. On this assumption, we are able to derive the volume fraction of non-icy material mixed with water ice throughout the C ring. We divided the C ring into eighteen 1,000 km-wide radial bins. For each radius bin, we derived the best-fit silicate fraction for each observation point within that radius range and take their average as the non-icy material fraction for that radius bin. The derived radial variation of non-icy fraction of each radius bin is shown in Fig. 14. We find that the silicate fraction reaches its maximum of ~6.3% by volume in the middle C ring. Away from its peak value, the material fraction decreases gradually inward, but much more strongly outward of ~83,000 km. The grey lines show the range of one standard deviation, for each radial bin.

We find fairly large uncertainties. There are a couple of reasons for this: (1) because we are limited by the radial resolution of our observation (~2000 km), we aren't able to resolve the radial variation of the non-icy material fraction on smaller radial scales; (2) the Mie scatter phase function is an approximation that fits the overall observation profile shape well, but when it comes to each observation point, data at certain azimuthal angles may deviate from the Mie scatter profile by some small amount; (3) Observational uncertainties might also cause these deviations which will then cause uncertainties in the amount of the intrinsic thermal emission, and therefore the non-icy material fraction; and, (4) considering that the non-icy material fraction shouldn't be polarization-dependent, we have combined all data from the three different polarizations. Yet, we see that there is a slight difference

in the observations at different polarizations (see Sec. 2). However, our Monte Carlo code is not able to deal with polarized light. The difference between different polarizations also increases the deviation. Despite these uncertainties, the increased non-icy material fraction in the middle C ring remains a statistically robust result.

## 5. Interpretation & discussion

The radial variability of the derived non-icy material fraction is surprising and warrants discussion. We expect that after their formation, the rings have been continuously polluted and darkened by extrinsic meteoroid bombardment. The nominal one-sided incident micrometeoroid flux on a flat plate (*i.e.*, flux at “infinity”) is given by  $\dot{\sigma}_\infty = 4.5 \times 10^{-17} \text{ g cm}^{-2} \text{s}^{-1}$  before being affected by gravitational focusing (Morfill et al., 1983; Cuzzi and Estrada, 1998; Estrada et al., 2015). For the gravitational focusing by the planet, we use the expression:  $F(r) = F_G(r/1.8 R_S)^{-0.8}$ , where the planet’s focusing is numerically averaged into the factor  $F_G$  at a reference radius  $1.8 R_S$ , and the radial dependence is a numerical fit to the calculated focusing of Durisen et al. (1992). In this paper we adopt a value of  $F_G = 3$ , appropriate for Oort cloud projectiles (Cuzzi and Estrada, 1998). The two-sided incident flux of material crossing the ring plane at ring radius  $r$  is then  $\dot{\sigma}_e(r) = 2F_G(r/1.8R_S)^{-0.8}\dot{\sigma}_\infty$ . However, only a fraction of these incident meteoroids impact the rings as they pass through them with an impact probability  $\varsigma$  that depends on the local geometric optical depth  $\tau_{\text{geometry}}$ :

$$\varsigma = \left(1 - e^{-(\tau_{\text{geometry}}/\tau_s)^P}\right)^{1/P}. \quad (17)$$

where  $\tau_s = 0.515$ , and  $P = 1.0335$  (Cuzzi and Estrada, 1998). The geometric optical depth is related to the optical depth given in Eq. (11):  $\tau_{\text{geometry}} = \int_{a_{\min}}^{a_{\max}} \pi a^2 \cdot n(a) da$  and  $\tau_{\text{geometry}} \sim 1/2\tau_{\text{optical}}$  ( $\lambda = 2.2 \text{ cm}$ ). Together, this gives the local impacting flux:  $\dot{\sigma}_{\text{im}}(r) = \varsigma \dot{\sigma}_e(r) = 2\dot{\sigma}_\infty \varsigma F(r)$ . The exposure time scale due to micrometeoroid bombardment is inversely proportional to this impact flux (Sec. 5.1). However, the absolute time scale derived from this is complicated by existing uncertainties in the flux and the assumed source of the micrometeoroid population (Estrada et al., 2015). Recently though, results of the Cassini Cosmic Dust Analyzer (CDA) have been reported that appear consistent with the current value of the flux at infinity, but also indicate that the population of micrometeoroids are not cometary in origin (Altobelli et al., 2015, also see Sec. 5.4). Thus the amount of gravitational focusing by Saturn may be different. In such a case, the time scales we report in this paper associated with micrometeoroid bombardment and ballistic transport can be scaled accordingly.

Considering that the gravitational focusing only has a somewhat weak radial dependence within the C ring, the local impacting flux depends approximately linearly on the local geometric optical depth in most regions of the C ring. The final non-icy material fraction is then inversely proportional to the local surface density. This implies that in the optically thin C ring, the non-icy material fraction should be determined by opacity, which equals geometric optical depth divided by surface density ( $\kappa = \tau_{\text{geometry}}/\sigma$ ). The larger the opacity, the higher the non-icy material fraction should become. Though a complete opacity radial profile for the C ring is still unknown, the current values at a few radial locations from density wave measurements suggest a higher opacity in the inner (and outer) C ring of  $\sim 0.15 \text{ cm}^2 \text{ g}^{-1}$ , and a significantly lower opacity in the middle C ring of  $\sim 0.022 \text{ cm}^2 \text{ g}^{-1}$  (Baillie et al., 2011; Hedman and Nicholson, 2013; see the diamonds and circles in Fig. 17), which is the opposite trend to the shape of the non-icy material fraction we have found. Therefore, if the impacting micrometeoroid flux is the only source of pollution, it would generate a non-icy material fraction profile in the C ring opposite to what is

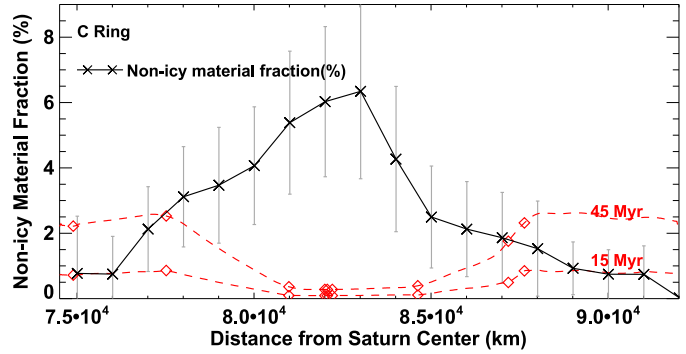


Fig. 15. Black curve: Derived non-icy material fraction from the observations. Red dashed curve: The non-icy material fraction evolution over 15 and 45 Myr, if meteoroid bombardment is the only source of contamination in a structurally fixed ring, and the flux has remained constant over the past tens of millions of years. Red diamonds demonstrate the positions where opacity measurements (Baillie et al., 2011; Hedman and Nicholson, 2013) have been made through density waves.

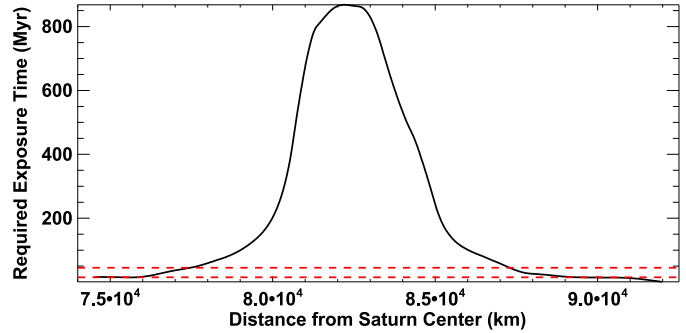


Fig. 16. Radially varied, required exposure time to accumulate the derived non-icy material fraction from direct deposition due to meteoroid bombardment. The red dashed lines correspond to 15 and 45 million years.

observed: a higher fraction outside the middle C ring bump, and lower at its center assuming the optical depth has also remained constant over this time.

In Fig. 15, we demonstrate how the non-icy material fraction would evolve over 15 Myr and 45 Myr after the C ring first formed assuming that the rings were initially pure water ice, that meteoroid bombardment is the only pollution source and that the C ring optical depth and surface density have not changed significantly during that time. The non-icy material fraction originating from meteoroid bombardment is determined by the local opacity. However, as we have already indicated, we only have opacity measurements in a few radial locations (see the red diamonds, Fig. 15). For now, we interpolate the opacity in between these measured values, but acknowledge that future measurements will be required in order to determine the true opacity profile. The opposite trend between the observed (black curve) and simulated (red dashed curve) non-icy material fraction profiles in Fig. 15 implies that if the rings started as mainly pure ice  $\sim 15\text{--}45$  Myr ago, there must be some non-icy material source other than the nearly radially constant micrometeoroid flux in order to explain the enhanced non-icy fraction in the middle C ring.

We also show the required exposure time as a function of ring radius for the same models in Fig. 15 in order to accumulate the observed non-icy material fraction merely from meteoroid bombardment at all C ring radius (see Fig. 16). This gives an upper bound on the age required to match the peak non-icy material fraction value at the center C ring of  $\sim 900$  Myr, with the assumption that the C ring optical depth and surface density has not changed significantly during that time. However, if this is the case,

it would imply that the non-icy material fraction in the inner and outer C ring would be much higher than the observed values and a process that preferentially removes non-icy material from the inner and outer C ring regions would be required in order to account for the observed distribution. The possibility of this scenario is discussed in Sec. 5.3.

Another alternative is that the C ring did not start out as nearly pure ice. In such a case, if the non-icy material was intramixed within the initial ring composition, any radial variability that may have existed most likely would have already been smoothed out as a result of ballistic transport (Cuzzi and Estrada, 1998; Estrada et al., 2015), given the nominal value for the micrometeoroid flux. That is, ballistic transport, which behaves much like both a diffusive and advective process (Cuzzi and Estrada, 1998; also see Sec 5.1), generally works to smooth out any compositional differences that may have existed or that might arise in the rings. Indeed, how material is diffused/advedted through ballistic transport in the rings is an effective means by which the age of ring features or the rings themselves can be determined. Therefore, the exceptionally high non-icy material fraction in the middle C ring requires either the recent introduction of a high concentration of non-icy material, or a process that preferentially removes non-icy material from the inner and outer C ring regions. We argue that the persistence of a non-uniform distribution of silicates within the middle C ring strongly favors the former scenario. In the next sections, we describe several scenarios in more detail that attempt to address this observation.

### 5.1. A band of Non-icy material from an impacting centaur at C ring center

In the first scenario, we assume that meteoroid bombardment has continuously contaminated the whole of the C ring since it first formed (see the above discussion), and that a higher concentration of non-icy material was injected into the middle C ring at a more recent time. Due to the lack of a complete opacity profile, it is not possible to determine the direct deposition timescale (red dashed curves, Fig. 15) that matches the observed non-icy fraction for the low optical depth regions away from the middle C ring peak, but barring any process that might dilute the non-icy fraction (e.g., a by-product of ballistic transport is that icier material spills over from the B ring to C ring; Durisen et al., 1992; Estrada et al., 2015), the implied age of the C ring from this evolution is between 15 and 45 Myr based only on the pollution of the inner and outer C ring for the nominal micrometeoroid flux (see Fig. 15). Note that this estimate is inversely proportional to the time-averaged micrometeoroid flux.

Any additional contribution to the effective dielectric constant of material must be attributed to an alternative, more localized source. In order to further examine this source, we investigated a scenario in which the middle C ring was contaminated by a debris cloud derived from a Centaur disrupted by previous encounters with Saturn (Hedman et al., 2011). Centaurs captured into orbit around Saturn might break apart into debris through tidal disruption as they pass close to the planet, or even through direct collision with the rings. This debris will follow the same bound trajectory and crash into the rings potentially across a range of radii at later periapses (Hedman et al., 2011). Assuming the non-icy material is all silicates, and that this material is now finely ground and intramixed within the ring particles, we find that the total mass of silicates in the debris cloud would need to be between  $\sim 4.3 \times 10^{15} - 4.8 \times 10^{15}$  kg in order to produce the observed non-icy material distribution in the middle C ring, with the mass range depending on the age of the C ring (15 – 45 Myr) as determined by our model fit to the low  $\tau$  regions. Considering that the water ice fraction in Centaurs might range from 0% to 40%, this debris may

therefore be produced during the break-up of a Centaur with radius  $R \sim 7 - 11$  km. The capture of the Centaur would likely involve it passing through the ring plane several times leaving little material behind initially, becoming weaker and rubblized until tides break up the object into smaller fragments which could then be captured and integrated into the rings (Hyodo and Ohtsuki, 2014). In such a scenario, it is not clear that the material would initially be concentrated into a narrow annulus of material. However, in the case that a narrow annulus is the initial condition, the spreading timescale of the high concentration of non-icy material through ballistic transport (Cuzzi and Estrada, 1998) could help constrain the earliest possible time the initial contamination occurred.

A conservative estimate of the lower bound on the spreading time scale for a concentration of non-icy material may be obtained by considering that ballistic transport can be approximated as an advective process in which the “bulk flow” is in the direction of ejecta material transport (Cuzzi and Estrada, 1998). Under this assumption, the time  $t_{\text{lim}}$  it would take for the intramixed pollutant that initially occupies an annulus at  $\sim 83,000$  km to spread into the observed distribution then is given by:

$$t_{\text{lim}} \sim \frac{\Delta r}{\delta} t_{\text{BT}} \sim 150 t_g. \quad (18)$$

Here,  $\Delta r = 9000$  km and the throw distance of impact ejecta  $\delta = 4rv_{\text{ej}}/\nu_k \sim 10^{-3}R_s \sim 60$  km, where we have taken the velocity of the bulk of ejecta to be  $v_{\text{ej}} \sim 4 \text{ m s}^{-1}$ . The ballistic transport time scale  $t_{\text{BT}} \sim t_g$  (the gross erosion time), is defined as the time a reference ring annulus of surface density  $\sigma$  would disappear due to ejected material if nothing returned:

$$t_g(r_0) = \frac{\sigma(r_0)}{\dot{\sigma}_{\text{ej}}(r_0)} \approx 6.22 \times 10^4 \text{ years}. \quad (19)$$

where the ring surface density is  $\sigma(r_0) = 5.3 \text{ g cm}^{-2}$  at  $r_0 = 83,000$  km (Hedman and Nicholson, 2013). The ejected mass flux  $\dot{\sigma}_{\text{ej}}$  is proportional to the impacting micrometeoroid flux times the ejecta yield  $Y_0$ , and is given by  $\dot{\sigma}_{\text{ej}}(r) \approx 2\dot{\sigma}_{\infty}\zeta F(r)Y_0$ . We take the mass ejecta yield  $Y_0 = 10^4$  and thus have  $\dot{\sigma}_{\text{ej}}(r_0) \sim 5 \times 10^{-14} \text{ g cm}^{-2} \text{s}^{-1}$ . For an initially narrow annulus of pollutant at 83,000 km, the time to spread to the observed width  $\Delta r \sim 9,000$  km is  $\sim 9.3$  Myr. Therefore the non-uniform radial peak in our intramixed, non-icy material fraction profile would be a relatively new structure, with an age on the order of  $\sim 10$  Myr, though the absolute time scale depends on the meteoroid flux rate at infinity and how gravitationally focused the micrometeoroids are by Saturn (Sec. 5).

Such Centaur crossing events are fairly likely to occur over this time period. According to numerical simulations (Horner et al., 2004), there is on average one centaur ( $R > 1$  km) that impacts Saturn every  $2.8 \times 10^4$  years, and thus based on this work we estimate that more than 350 Centaurs have had the opportunity to impact Saturn in the past  $\sim 10$  Myr (though there is some evidence this may be an underestimate, see Hedman et al., 2011; Marouf et al., 2011). In order to find the fraction of Centaurs with radius  $R$  larger than 7 km among them, we investigate the absolute magnitude  $H$  distribution of observed Centaurs, which is related to their radius as:

$$R = \frac{1329 \text{ km}}{2\sqrt{p}} 10^{-0.2H}. \quad (20)$$

where  $p$  is the typical Centaur geometric albedo (e.g., Chesley et al. 2002). For this calculation, we adopted the median value for the measured Centaur albedo of  $p = 0.07$  (Johnston, 2015). The observed Centaurs have  $H$  between 6 and 14.3, with the absolute magnitude  $H$  distribution law  $N(< H) \sim 10^{0.54H}$  (Larsen et al. 2001; Di Sisto and Brunini 2007). The fraction of Centaurs with radii greater than the required impacting radius ( $R > 7$  km) is  $\sim 15\%$ .

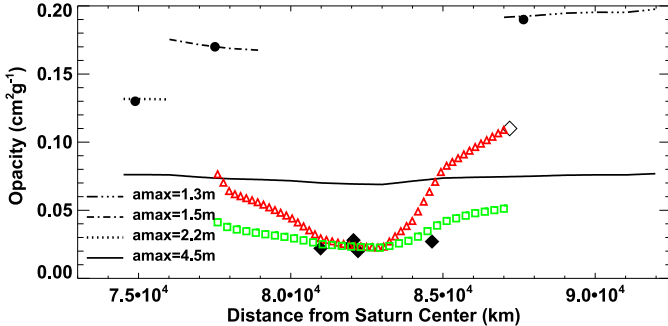


**Fig. 17.** Measured opacity using density waves. Circles are from Baillie et al. (2011) and diamonds are from Hedman and Nicholson (2013). Filled symbols are measurements outside the plateaus while the unfilled points are measured inside the plateaus. Opacities calculated with different maximum particle size are presented by different line types. In all these calculations, the same minimum size of 0.4 cm and power law index  $q = 3.15$  is applied. The suggested 75% porosity and the derived radially-varying fraction of silicates are also applied to the four cases with different maximum size. Also plotted are the opacity profiles in the middle C ring using the silicate-core, porous-icy-mantle model (described later in Sec. 5.2, refer to Fig. 20). Green squares: opacity profile for radially-varying percentage of large particles containing a silicate core. Red triangles: opacity profile for a radially-varying maximum particle size in the silicate-core, porous-icy-mantle model. (For interpretation of the references to colour in this figure legend, the reader is referred to the web version of this article.)

Therefore, on average,  $\sim 52$  Centaurs larger than 7 km in radius may have hit Saturn within the last  $\sim 10$  Myrs. Even if we extend the range of Centaur absolute magnitude to  $5 < H < 16.2$  (Di Sisto and Brunini, 2007), there would still be  $\sim 5$  Centaurs larger than 7 km impacting Saturn within the given time frame.

This estimate only considers those objects that impact with Saturn. We expect that an even larger number of them may have passed close enough to the planet to be significantly affected by the planet's gravitational well and might have been broken up into debris. Once the Centaur is disrupted into debris by Saturn's gravity, the debris is likely to be absorbed by the rings after several orbits. The observational evidence would suggest, however, that successful disruption and capture events of such large Centaurs have not happened so frequently otherwise we might expect to see relatively large peaks in non-icy material concentration in other C ring regions rather than the single, well-defined peak we observe in the middle C ring.

## 5.2. Ring opacity favors large rocky chunks

In section 5.1, we have discussed the case where non-icy material brought in by the incoming Centaur is intramixed within the ring particles as envisioned in the Effective Medium Theory (EMT) model. However, it seems unlikely that an incoming Centaur, basically a rocky object which may have substantial internal strength, torn apart gently by tides and ultimately broken into pieces that reside in the C ring, could be ground to powder this way, especially if it were done fairly recently. It seems more likely that there would still be many chunks of solid silicates in the centimeter-decimeter-meter size range left, which have now been coated by the icy ring material. This would require more total non-icy material in the middle C ring since non-icy material affects emission most efficiently when finely divided as in the EMT intramixed assumption versus a “salt and pepper”, or intramixing type model (e.g., Cuzzi and Estrada, 1998; Poulet and Cuzzi, 2002; Cuzzi et al., 2014).

Moreover, 75% porous ring particles containing less than 7% intramixed non-icy material implies a ring layer opacity of  $\sim 0.07 - 0.08 \text{ cm}^2 \text{ g}^{-1}$  (see solid black curve, Fig. 17, also see Fig. 20) using our nominal particle size distribution, which is in-

consistent with the density wave measurements. Surface density measurements have been made at several locations in the C ring where density waves are present (Baillie et al., 2011; Hedman and Nicholson, 2013). The opacity  $\kappa$  can be derived from these measurements (see black diamonds and circles, Fig. 17) using

$$\begin{aligned} \kappa &= \frac{\tau_{\text{geometry}}}{\sigma} = \frac{\int_{a_{\min}}^{a_{\max}} n(a) \cdot \pi a^2 da}{\int_{a_{\min}}^{a_{\max}} \bar{\rho} \cdot n(a) \cdot \frac{4\pi}{3} a^3 da} \\ &= \frac{3(4-q)}{4(3-q)} \cdot \frac{a_{\max}^{3-q} - a_{\min}^{3-q}}{a_{\max}^{4-q} - a_{\min}^{4-q}} \cdot \frac{1}{\bar{\rho}}. \end{aligned} \quad (21)$$

Recall that the derived radial opacity profile from density wave measurements is notably non-uniform, with a value in the middle C ring of  $\sim 0.022 \text{ cm}^2 \text{ g}^{-1}$ , which is much lower than in the inner and outer C ring. According to Eq. (21), in order to have a radially-varying opacity profile, the C ring particles must have a radially-varying particle size distribution or a radially-varying mean particle density  $\bar{\rho}$ .

Using the same particle size distribution throughout the C ring for the EMT model of section 3.3, the calculated opacity curve is fairly flat, since less than 7% non-icy material has little effect on the mean particle density. At the inner and outer C ring, the measured opacity is higher than our calculated value, possibly suggesting fewer large particles in those regions. We are able to match the measured opacity by decreasing the maximum particle size from 4.5 m to 1.5 m – 2.2 m in the inner C ring and 1.3 m in the outer C ring (see Fig. 17). These changes would not much affect our previously simulated scattered light component for the occultation and non-occultation data, since surface density and opacity mainly depend on the large particles, while small particles dominate the scattering properties. However, by merely increasing the maximum particle size it is still not possible to lower the opacity in the middle C ring to the measured value, because it would require the maximum size to be  $\sim 25$  m, incompatible with Voyager RSS estimates of the particle size distribution by Zebker et al. (1985). Thus, we conclude that the exceptionally low opacity in the middle C ring suggests a potentially considerable amount of extra mass hidden in the ring particles, just where the finely distributed non-icy material also is.

To address the scattering behavior of particles containing large chunks of silicates, we expect to do more detailed modeling with a discrete dipole approximation (DDA) code in a future paper. For now, we consider a uniform core-mantle model using a silicate-rich core and dirty-ice mantle in order to gauge its effectiveness in matching the observations. In this simplified model, we assume that the composition of the background C ring is primarily water ice, but with a fraction of  $\sim 1\%$  non-icy material (as in Fig. 14) which is assumed to be intramixed within ring particles that have 75% porosity. We also assume a critical size  $a_{\text{crit}}$  for the population that includes the Centaur fragments such that particles smaller than this critical size have a composition similar to the background, while particles larger than this contain a silicate core covered with a porous dirty icy mantle that has the same non-icy fraction and porosity as the background C ring particles. To further simplify the model, we also assume that the ratio of silicate core radius to particle radius  $f_r$  is fixed for all core-containing particles.

We can estimate the best value of the critical particle size and the core radius ratio to match our observations by considering the two main characteristics in our data that we need to match: high brightness temperature in the occultation data and large thermal emission in the middle C ring. The large occultation brightness is determined by the integrated phase function, which must scatter more light into small scattering angles. The effective anisotropy

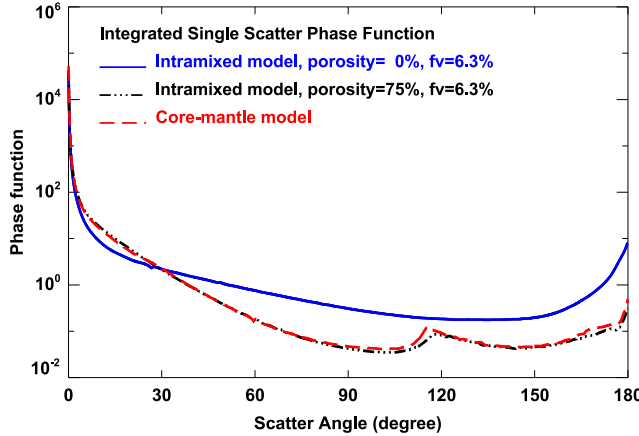


**Fig. 18.** Single scattering phase function integrated over the C ring particle size distribution for three models. Nominal particle size distribution is applied to all three cases. Model 1 (blue) silicate intramixed with water ice; zero porosity. Model 2 (black): silicate intramixed with water ice; 75% porosity. Model 3 (red): silicate-core icy-mantle model with  $a_{\text{crit}} = 60$  cm, and the core radius ratio equals  $f_r \sim 0.65$ . (For interpretation of the references to colour in this figure legend, the reader is referred to the web version of this article.)

factor is given by

$$g_{\text{eff}} = \frac{\int_{a_{\min}}^{a_{\max}} \left( \int_0^\pi P(\theta, \phi) \cos\theta \sin\theta d\theta \right) Q_{\text{sca}}(a) \pi a^2 n(a) da}{\int_{a_{\min}}^{a_{\max}} Q_{\text{sca}}(a) \pi a^2 n(a) da}. \quad (22)$$

where  $P(\theta, a)$  is the phase function at scattering angle  $\theta$ , for a particle of radius  $a$ . A larger value of  $g_{\text{eff}}$  implies a more forward-directed phase function. As discussed in Section 4.1, we are able to match the low-resolution occultation observation by adding 75% porosity. For this value of the porosity, the effective anisotropy factor increases from  $\sim 0.6$  (when assuming zero porosity) to above 0.838. Therefore, the larger the anisotropy factor, the higher the brightness of our occultation observation would be. On the other hand, the integrated absorption coefficient

$$\alpha = \frac{\int_{a_{\min}}^{a_{\max}} Q_{\text{abs}}(a) \pi a^2 n(a) da}{\int_{a_{\min}}^{a_{\max}} Q_{\text{ext}}(a) \pi a^2 n(a) da}. \quad (23)$$

determines the amount of thermal emission emitted per particle on average. A ring layer with normal optical depth  $\tau$ , can generate a total amount of intrinsic thermal emission of  $\sim \tau_{\text{abs}} \cdot T_{\text{ring\_physical}} (\tau_{\text{abs}} \ll 1)$ , where  $\tau_{\text{abs}} = \alpha \cdot \tau$  is the absorption optical depth and  $T_{\text{ring\_physical}}$  is the physical temperature of the ring layer. At the peak of the middle C ring non-icy material fraction hump (see Fig. 14), for particles with 75% porosity and  $\sim 6.3\%$  non-icy material, Eqns. (22) and (23) imply that  $g_{\text{eff}} = 0.838$  and  $\alpha = 0.0626$ .

Our core-mantle model is simulated with a layered sphere Mie scattering code. We find that we obtain a similar effective anisotropy factor  $g_{\text{eff}} = 0.832$  and absorption rate  $\alpha = 0.0620$  when  $a_{\text{crit}} = 60$  cm, and the core radius ratio equals  $f_r \sim 0.65$ . These parameters give the observed value of the opacity at  $\sim 83,000$  km in the middle C ring of  $\sim 0.022 \text{ cm}^2 \text{ g}^{-1}$ . Similarly to Fig. 12, we investigate the integrated single scattering phase function of this silicate-core/icy-mantle model (see Fig. 18). The phase function of this model is very close to the intramixed model with 75% porosity, so it will not change the scatter component for the occultation and non-occultation data we simulated before.

In Fig. 19 we provide a quantitative fit to the radial variation of the non-icy fraction in the middle C ring hump between 78,000 km – 87,000 km, using our determined values for  $a_{\text{crit}}$  and  $f_r$ . In the left panel, we show a fit under the assumption that among all particles larger than the critical particle size, only a percentage of them contain a silicate core, and the percentage that contains a core is radi-

ally dependent on the distance from the peak. At the peak of the middle C ring non-icy material fraction hump ( $\sim 83,000$  km), the percentage is 100%. The percentage drops to  $\sim 45\%$  at 78,000 km, and  $\sim 20\%$  at 87,000 km (see green squares in Fig. 17 for the resulting opacity profile). In the right panel, we show a fit in which all particles larger than the critical size contain a silicate core, but adopt a radially-varying maximum particle size (see red triangles in Fig. 17 for the resulting opacity profile). In both of these fits for the core-mantle model, we determine that the pollution source would need to contain a mass of silicate material of  $\sim 9.8 \times 10^{16} - 1.07 \times 10^{17}$  kg, which corresponds to an object radius of  $R \sim 20-21$  km (for a silicate density of  $2.7 \text{ g cm}^{-3}$ ) in order to account for the amount of non-icy material the observations imply in the middle C ring hump. There would be  $\sim 3$  Centaurs larger than 20 km impacting Saturn within the past  $\sim 10$  Myr (see Sec. 5.1 for detailed calculation).

### 5.2.1. Viscous spreading of an initially high surface density annulus

Although ballistic transport can explain the radial distribution of the non-icy material fraction in the middle C ring through the spreading of an initially high concentration of finely ground pollutant that is intramixed within the ring particles (Sec. 5.1), it does not do well to explain the observed opacity in the middle C ring, whereas the core-mantle model can. This is because the latter ring particles are much denser than the former for any given particle size since most of the non-icy material is hidden within their interiors. Moreover, if the Centaur debris is initially in a narrow annulus in the form of chunks, then the bulk material must spread viscously in order to account for the observed opacity distribution.

The fits to the radial structure seen in Fig. 19 suggests that the Centaur debris was initially in a high surface density annulus centered at  $\sim 83,000$  km, which later viscously spread radially to a width  $\Delta r$  over time. A rough estimate of this viscous timescale is:

$$t_{\text{visc}} \sim \frac{\Delta r^2}{3\nu} \sim 2 \times 10^7 \left( \frac{\Delta r}{9000 \text{ km}} \right)^2 \left( \frac{300 \text{ cm}^2 \text{ s}^{-1}}{\nu} \right) \text{ yrs}. \quad (24)$$

where the estimate of the viscosity comes from the initial surface density contained in the annulus (see below). However, this estimate becomes increasingly unreliable as a predictor of the actual timescale because the viscosity  $\nu$  can drop sharply over time as the annulus spreads. Thus we consider a more detailed calculation to estimate the spreading time.

Under the assumption that the Centaur material is initially contained in a dense, narrow annulus, its evolution under the influence of viscosity can be modeled using (Pringle, 1981)

$$\frac{\partial \sigma}{\partial t} = \frac{3}{r} \frac{\partial}{\partial r} \left\{ r^{1/2} \frac{\partial}{\partial r} (r^{1/2} \nu \sigma) \right\}. \quad (25)$$

In a Keplerian, pressureless disk such as the rings, the viscosity responsible for angular momentum transport arises as a result of particle interactions and can be divided into contributions from particle random motions  $\nu_L$  (the “local” shear stress component, Goldreich and Tremaine, 1978), the momentum transferred from physical collisions  $\nu_{NL}$  (the “non-local” component, e.g., Araki and Tremaine, 1986) and for dense rings, gravitational scattering due to the presence of self-gravity wakes  $\nu_{\text{grav}}$  (e.g., Salo, 1992; Daisaka and Ida, 1999).

A simple prescription for the viscosity that can be applied to Eq. (25) that depends on whether the ring is gravitationally stable or not is given by (e.g., Salmon et al., 2010; also see Schmidt et al., 2009, for a detailed discussion)

$$\nu = \nu_L + \nu_{NL} + \nu_{\text{grav}} = \begin{cases} \frac{c^2}{2\Omega} \frac{0.46\tau}{1+\tau^2} + a^2 \Omega \tau & Q_T > 2; \\ 26(r_h^*)^5 \cdot \frac{G^2 \sigma^2}{\Omega^3} + a^2 \Omega \tau & Q_T \leq 2; \end{cases} \quad (26)$$

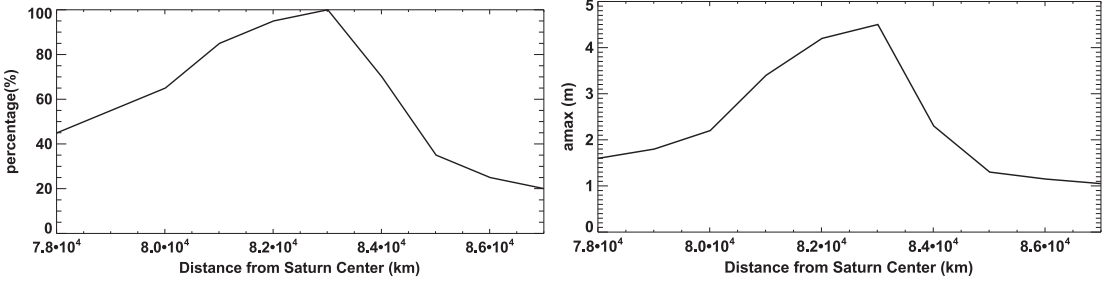


**Fig. 19.** Left panel: The radially-varying percentage of large particles (larger than the critical size  $a_{\text{crit}}$ ) that contain silicate cores necessary to match the observed anisotropy factor and absorption rate (Eqs. [22] and [23]). Right panel: The radially-varying maximum size.

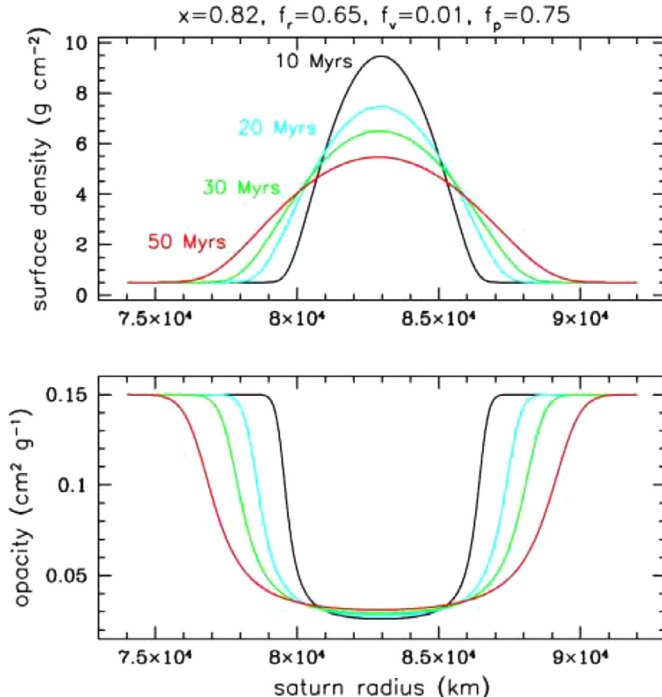


**Fig. 20.** Viscous spreading of an initially narrow annulus (50 km) over time. Upper panel: Surface density after 10 (black), 20 (cyan), 30 (green) and 50 Myrs (red solid curves). Lower panel: Corresponding opacity profiles. These simulations indicate that the surface density and width of the middle C ring bump can be achieved in as little as  $\sim 20$ – $30$  Myrs. (For interpretation of the references to colour in this figure legend, the reader is referred to the web version of this article.)

where  $Q_T = \Omega c / 3.36 G \sigma$  is the Toomre parameter which distinguishes between the gravitating ( $Q_T \leq 2$ ) and non-self gravitating ( $Q_T > 2$ ) regimes. The nondimensional factor  $r_h^* = r(\pi \rho / 9M_s)^{1/3}$  is the ratio of a particle's Hill sphere to its physical radius  $a$ , where  $M_s$  is the mass of Saturn, and the velocity dispersion  $c = 2a\Omega$  for  $r_h^* \leq 0.5$ , and  $c = \sqrt{Gm/a}$  for  $r_h^* > 0.5$  where  $m$  is the particle mass (see, e.g., Daisaka et al., 2001).

In Fig. 20 we show a simulation of the spreading of an initial annulus of width  $\Delta r = 50$  km derived from a  $R \approx 26$  km Centaur composed of rock and ice with a silicate mass fraction of 82%, giving it a density of  $1.43 \text{ g cm}^{-3}$  and mass  $\approx 1.1 \times 10^{17} \text{ kg}$ , respectively. The rocky chunks are assumed to be relatively large so the size distribution within the annulus is taken to have a minimum size (rock+ice) of  $a_{\text{crit}} = 60 \text{ cm}$ , and a maximum size of  $450 \text{ cm}$ . The mass of additional ice brought in by the Centaur is chosen so as to be consistent with particles that have a core-to-particle radius ratio of  $f_r = 0.65$ , with porous, dirty icy mantles that have a porosity of  $f_p = 0.75$  and an intramixed fraction of silicates of  $f_v$

= 0.01 (see above).<sup>1</sup> The background C ring is assumed to be made up of icy, porous particles with our nominal choice of parameters for the size distribution (see Sec. 3.3) except that the maximum particle size has been reduced to 2.2 m as described earlier in this section in order to match the opacity in the inner C ring. In determining the viscosity in Eq. (26), we calculate the relevant quantities by finding mass average weighted means integrated over the size distribution.<sup>2</sup> This gives, for example, a more conservative estimate of the velocity dispersion  $c$  than assuming it were determined by the largest particle size  $a_{\text{max}}$ .

In the upper panel we show the evolution of the surface density. The initial surface density in the annulus is  $\sigma \approx 420 \text{ g cm}^{-2}$ , which for our parameter choices gives an initial value for  $Q_T < 2$ . However, this is short lived as the annulus spreads quickly and the local and non-local contributions to the viscosity dominate the evolution. We find that we can roughly match the observed width ( $\sim 78,000 \text{ km} - 87,000 \text{ km}$ ) and peak surface mass density of the middle C ring feature within  $\sim 20 - 30$  Myrs. In the bottom panel, we show the associated ring opacity which is characterized by a broadening, deep dip in opacity similar to what is seen in the observations. As pointed out earlier, the opacity in the middle C ring is satisfied in this model for the choices of the core fraction  $f_r$  and critical particle size  $a_{\text{crit}}$ . Although our simulation is idealized, this relatively simple model indicates that a captured object such as a disrupted Centaur that is initially contained within a narrow annulus in the middle C ring could account for the observed dynamical ring profile, with the Centaur capture occurring as little as  $\sim 20$ – $30$  Myrs ago.

### 5.3. Alternate scenarios

#### 5.3.1. Tidal or catastrophic breakup of fragments of saturnian origin

An alternative source for the high silicate fraction in the middle C ring may be from a rocky fragment that originated from the breakup of one or more of the Saturnian moons. This could occur from either tidal disruption, a catastrophic impact with a heliocentric interloper or possibly even a collision between mid-sized (or larger, see Asphaug and Reufer, 2013) satellites. For example, Canup (2010) suggested that the rings could have formed from the tidally stripped mantle of a Titan-sized differentiated satellite at the tail end of satellite formation. On the other hand, Charnoz et al. (2009b) have argued that the most likely time in which a moon near the Roche limit of the planet could be disrupted would be at the Late Heavy Bombardment (LHB). A Rhea-sized moon could serve as the progenitor for the rings, while also spinning off

<sup>1</sup> We note that the ice for the mantles could have come from the C ring itself. In such a case, we could consider a Centaur of pure rock that would be 20 km in radius.

<sup>2</sup> Note that the model of Daisaka et al. (2001) only treats a single particle size  $a$  which does not actually appear in the expression for  $v_{\text{grav}}$ . Thus in this term the viscosity is determined through the surface density only.

several mid-sized satellites we see today (Crida and Charnoz, 2010, 2012). A critique of these models is the whereabouts of the rocky content of these moons, in particular the core. However, given the compositions of the mid-sized satellites, the ring progenitor could have been predominantly icy, though it then becomes difficult to explain the rocky fractions of the current satellites in this picture. Charnoz et al. (2011) explained the silicate fractions of the satellites and predominantly icy rings with their models and argued that any remaining silicates would be isolated within the rings in larger chunks coated with ice.

As a consequence of tidal or catastrophic disruption, it may not be unreasonable to consider that there could have been large fragments with high non-icy material fraction that found their way into the C ring, especially if the moon was internally non-uniform (e.g., itself the product of a previous breakup and reaccretion event). On the other hand, a mostly rocky fragment may have been deposited in the already existing rings as a result of the subsequent evolution of debris from a catastrophic collision between mid-sized moons. Depending on the internal strength of the object (*i.e.*, a rubble pile versus a solid fragment), the fragment may itself eventually be tidally disrupted or broken up catastrophically due to an impact with an object of heliocentric origin. In either case, a necessary requirement is that the object must be broken down completely to sizes in the decimeter-to-meter range.

The main difficulty with this scenario is that in order to introduce the extra amount of non-icy material we observe at the C ring center, the object would need to be at least  $R \sim 20$  km (assuming the object is pure silicate, see Sec. 5.1). Such an object is almost certainly stronger than just self-gravitating and thus if embedded intact within the ring would require a hypervelocity impact with a sufficiently large interloper to completely disrupt. An estimate of the size needed can be ascertained by equating the object mass  $M$  times the fragmentation energy per unit mass (in the gravity regime),  $Q^*_D$ , needed to disrupt an icy body (Leinhardt and Stewart, 2009)

$$Q^*_D \approx 26 \left( \frac{R}{1\text{km}} \right)^{1/3} \left( \frac{v}{1\text{km}\cdot\text{s}^{-1}} \right)^{0.7} \text{J}\cdot\text{kg}^{-1}. \quad (27)$$

to the kinetic energy of impact. This gives  $R_{\text{im}} = R(2Q^*_D/v^2)^{1/3}$ . A reasonable choice for the impact velocity is  $v \sim \sqrt{3} v_{\text{orb}} \sim 37$  km  $\text{s}^{-1}$ , where  $v_{\text{orb}}$  is the orbital velocity at a distance of 83,000 km from Saturn. This yields the requirement that the impactor size be  $\gtrsim 0.58$  km. Zahnle et al. (2003) have calculated impact rates onto Saturn and the known moons outside the rings. A similar calculation for the C ring fragment gives a time scale for which one would expect such a disruption on the order of  $\sim 3.8$  Gyr. This is longer than what can be inferred from Zahnle et al. for moons outside the rings in part because for a very flat impactor size distribution, the probability of disruption decreases for decreasing moon size since the number of projectiles large enough to disrupt them increases more slowly than the surface area of the moon decreases (Dones, priv comm).

The problem then is that it becomes very difficult to explain the observed distribution of non-icy material in the middle C ring over these long time scales. If the material is in large chunks, any compositional (and concentrated surface density) features would likely have been smoothed out due to viscosity, whereas if the material were well mixed within the ring particles, ballistic transport would have largely smeared out compositional differences. Thus, a satellite disruption event would probably have needed to happen within the last  $\sim 100$  Myr in order to be a viable alternative. However, this significantly decreases the probability of such a disruptive impact happening to  $\lesssim 3\%$  in that time frame.

One possibility for such a recent event may come as a consequence of a tidal dissipation factor of Saturn that is an order of magnitude smaller than originally thought as suggested by

Lainey et al. (2010; 2012). Though quite controversial, such a low value implies that the entire mid-sized satellite system may evolve rather quickly, and that it is an even more collisional (stochastic) system than previously thought. Several workers have already considered the ramifications of such a low tidal dissipation factor (e.g., Charnoz et al., 2011; Cuk et al., 2016). Cuk et al. (2016; also Cuk 2014) have investigated the evolution of the current mid-sized satellites numerically back in time and have concluded that as a result of the more rapid evolution of the system, a relatively recent breakup and re-accretion event of some of Saturn's mid-sized moons (inside the orbit of Rhea) may have likely occurred on the order of  $\sim 100$  Myr ago. Interestingly, the collision of these moons could potentially push a close-in, inner (perhaps Mimas-sized) satellite into Saturn's Roche zone via tidal interaction with the resultant debris disk, where it could subsequently be disrupted leading to the formation of the rings. The age of the rings we see then would be consistent with this breakup event timescale, while their mass could also be consistent with a recent estimate for the rings' mass through density waves in the B ring (Hedman and Nicholson, 2016). Although this presents an intriguing scenario, the remaining uncertainty with the value of Saturn's tidal dissipation factor as well as the relatively low probability of disruption of an embedded moon makes the Centaur capture model more likely.

**5.3.1.1. Removing non-icy material from the inner and outer C ring.** As an alternative to introducing an additional external non-icy source into middle C ring, we consider a process that preferentially removes non-icy material from the inner and outer C ring regions. If we imagine a scenario in which the C ring originally had a constant optical depth and surface density across its radial extent similar (or even initially larger) to what is currently observed in the middle C ring, then because meteoroid bombardment is nearly radially uniform, we would expect a roughly constant non-icy material fraction everywhere within the ring. As suggested by Fig. 16, it would take  $\sim 900$  Myr to accumulate a radially-uniform 6% non-icy material from meteoroid bombardment using the current accepted flux value. On the other hand, if we use the current optical depth and surface density profile, the non-icy fractions would actually be even *higher* in the lower optical depth inner and outer C ring, relative to the middle C ring. In either case, in order to match the observed distribution, there would need to be mechanisms at work that either acted to preferentially remove the non-icy material from the inner and outer edges, or diluted the pollutant in those regions through the introduction of icy material.

The outer parts of the C ring may be more straightforward to explain. A by-product of the ballistic transport process across the inner B ring edge is that icier material spills over from the B ring into the C ring. For example, the ramp that connects the inner B ring to the C ring comes about due to advective effects (Durisen et al., 1992; Estrada et al., 2015). It has been shown that the ramp has a color and albedo similar to the B ring (Cooke, 1991; Cuzzi and Estrada, 1998). Therefore, as a result of this material exchange process, the C ring may "lose" polluting material faster than it gains it, and the relatively sharp drop off in non-icy material fraction seen outside of  $\sim 83,000$  km (see Fig. 15) may be due to a steady stream of icy material drifting radially inward.

On the other hand, the inner C ring is more problematic. As shown in Fig. 15, the non-icy material fraction drops off much more gradually inside of  $\sim 83,000$  km than outside, and then noticeably flattens out inside of  $\sim 76,000$  km. This cannot be explained by the dilution mechanism described above. It so happens that this is around the location where part of the radar main beam starts to fall on the outer D ring while at the same time the optical depth becomes very small and uncertain at the C/D boundary, which may incur some error in our analysis. Moreover, in our Monte Carlo simulations we assume that the C and D ring particles

are exactly the same, which might be inaccurate. Since the flux at the C/D boundary is very low, these errors might cause a high uncertainty as to whether the magnitude of the non-icy material at the inner edge of the C ring is correct. If this were indeed an artifact, then it is possible that the radial non-icy material fraction profile does not drop off as significantly at the inner edge; however, one would still require some as-of-yet unknown mechanism to explain the lower fraction interior to the middle C ring.

Finally, a mechanism that may work by itself, or in conjunction with the dilution process in the outer C ring concerns the recent discovery of ring rain onto Saturn's ionosphere (Donoghue et al., 2009) which may possibly verify the previously suggested planet-to-ring magnetic connection (Connerney et al., 1984; Connerney et al., 1986; Wilson et al., 1989; Northrop et al., 1987). Small, highly charged debris grains can escape the ring plane to Saturn along magnetic field lines from the C ring (Jontof-Hutter and Hamilton 2012a,b). The critical stability limit for small ionized water ice particles lies in the outermost C ring. As the ionized water ice within the critical stability limit becomes unstable and erodes away, the non-icy material fraction in the inner and mibubble C ring would increase, potentially providing another means by which the observed distribution can be explained. Furthermore, the critical stability limit would become closer to the rings' inner edge for particles with smaller charge to mass ratio. If the non-icy material has relatively smaller charge to mass ratio than water ice, only non-icy material at small ring radius could be possibly removed. Such a process would need to be investigated in more detail

#### 5.4. Other non-icy materials suggested by observations at other wavelengths

Observations at visible and near-IR wavelengths have revealed a dark reddish C ring, indicating the existence of other non-icy reddening materials like tholins (Cuzzi and Estrada, 1998), or hematite (Stillman and Olhoeft, 2008; Clark et al., 2012) that presumably have been further polluted over time by some extrinsic darkening material. In the case of tholins, for example, the darkening agents were spectrally neutral such as amorphous carbon (Cuzzi and Estrada, 1998). But other extrinsic materials are possible, and can even be reddish themselves in nature (Cuzzi et al., 2009) indicating that the issue of ring composition still remains unsettled. Indeed, some silicates may likely have been present in the rings from their beginning (e.g., originating from a progenitor moon), but the idea of different materials like silicates, which we consider in this paper as the source of the rings' intrinsic thermal emission, also as extrinsic pollutants has been bolstered by the recent results of the Cassini CDA which determined that the micrometeoroid flux at Saturn is consistent with an Edgeworth-Kuiper belt origin (Altobelli et al., 2015; also see Sec. 5), and not cometary as has been previously assumed.

Regardless, considering the very small amounts of non-icy materials required to give the rings the right color in the visible and near-IR assuming it is intramixed within the ring particles (e.g., 0.35wt% of tholins, Cuzzi and Estrada, 1998; or 0.25wt% of nanohematite, Cuzzi et al., 2009; Clark et al., 2012), their contribution to the effective dielectric constant in the middle C ring can be considered insignificant with regards to the thermal emission. In addition, while using nanohematite as the reddening material, Clark et al. (2012) and Cuzzi et al. (2009) suggested using a small amount of un-oxidized, fine-grained iron instead of darkening material like silicates. As an example, in Fig. 21 we plot the magnitude of our derived imaginary part of the effective dielectric constant, which is required for the ring particles to generate the amount of the observed intrinsic thermal emission, as a function of ring radius (compare with Fig. 15). By adding 75% porosity to the ring particles, the real part of the effective

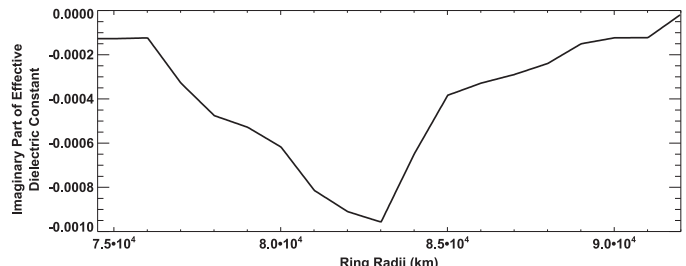


Fig. 21. Plot of the imaginary part of the effective dielectric constant required to match the thermal emission observed.

dielectric constant becomes about 1.45, using Eq. (14). However, if we assume un-oxidized iron as the non-icy material and plug its dielectric constant ( $\epsilon_{\text{iron}} = 0 - i \cdot 2 \times 10^6$ , Cuzzi and Pollack, 1978) into Eq. (14) (see Sec. 3.3), we cannot obtain the required imaginary part of the effective dielectric constant for the middle C ring even with as much as 80wt% iron, which is much larger than the amount of fine-grained iron suggested by these authors.

One can always determine the required fraction of any non-icy material by plugging its dielectric constant into Eq. (14), assuming that the non-icy material is intramixed within water ice. Then one can derive a radially varying non-icy material fraction profile and appropriate ring particle porosity by matching the imaginary part of the effective dielectric constant profile (Fig. 21) while keeping the real part near a value  $\sim 1.45$ . However, larger fractions of these candidate materials in the ring particles (e.g., tholins) needed to match the intrinsic thermal emission would be inconsistent with previously derived non-icy material fractions in the visible and near-IR. Therefore it is certain that even if the ring particles contain some of these other candidate materials which may dominate at shorter wavelengths (see below), there must be some other materials in the C ring such as silicates that primarily accounts for not only the thermal emission, but that can explain the anomalously low opacity in the middle C ring as well. We further point out that this is independent of, say, any uncertainty in the dielectric constant of silicates (of which naturally there are a whole range of "silicates" to choose from). Rather, any uncertainty in the fraction of non-icy material depends much more significantly on the choice of the non-icy constituent. Our analyses alone cannot determine the exact composition of the non-icy material; however, silicates represent a very reasonable candidate material, especially within the context of the newly determined micrometeoroid flux, and the Centaur capture scenario we have advanced.

Finally, we note that past analyses of visible and near-IR observations of the C ring have not indicated the presence of silicates in the fractions we derive in this work, mainly because even the very small amounts of spectrally red absorber (e.g., tholins) required to give the rings their apparent color would overwhelm these unless the silicates were present in much larger amounts (see Cuzzi and Estrada, 1998), even more than the enhanced values we find in the middle C ring. In any case, given the fact that the visible and near-IR can only penetrate through a very thin surface layer of the ring particles, the bulk of the larger fraction of silicates we find in the middle C ring are very likely to be hidden in the interior of the larger ring particles and not on their surfaces, as described by our silicate-core and porous-dirty ice mantle model.

#### 5.5. Discussion on composite ring particle mixing rules

The high particle porosity derived in section 4.1 is a surprising result. Initially we expected the ring particles to be mostly solid water ice with a small fraction of voids and non-icy material as inclusions. Thus, we used the Maxwell-Garnett mixing rule of the

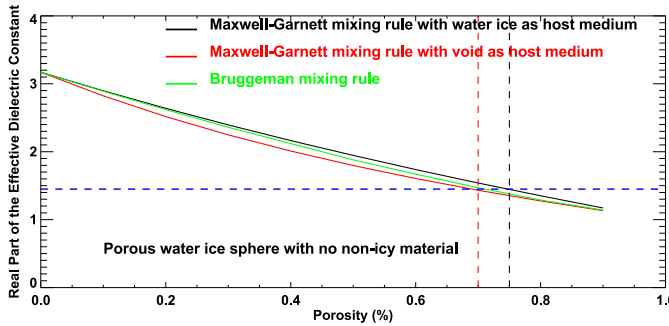


**Fig. 22.** The real part of the ring particle effective dielectric constant as a function of porosity using three different mixing rules: Bruggeman mixing rule (green), Maxwell-Garnett mixing rule with water ice (black) or vacuum as the host medium (red). (For interpretation of the references to colour in this figure legend, the reader is referred to the web version of this article.)

Effective Medium Theory (EMT) to calculate the ring particle's averaged (effective) dielectric constant taking water ice as the host medium. This mixing rule treats one material as the matrix (host material) in which other materials (guest materials) are embedded in the form of small inclusions. However, this model is not symmetric as the host and guest materials do not contribute on an equal basis to the effective dielectric constant. Therefore, it makes a difference what one chooses as the host material. For example, Cuzzi and Estrada (1998) used a vacuum as the host medium. Here, we investigate how significant the differences are when choosing different media and compare the results with the symmetric Bruggeman (1935) mixing rule.

To match the high brightness in the occultation data, we have increased the forward-scattered light by decreasing the real part of the ring particle dielectric constant to  $\sim 1.45$ . By using the Maxwell-Garnett mixing rule with water ice as the host material, we are able to match the required real part of the dielectric constant after making the ring particles 75% porous. In Fig. 22, we show the calculated real part of the effective ring particle dielectric constant as a function of the porosity for three different mixing rules: the Bruggeman mixing rule (green curve), the Maxwell-Garnett mixing rule with water ice (black curve), or vacuum (red curve) as the host medium. We find a slight difference of less than 0.2 in the real part of the effective dielectric constant when using water ice or vacuum as the host material in the Maxwell-Garnett mixing rule. The result of the Bruggeman mixing rule lies in between them. Furthermore, we find that the small non-icy material fraction (less than 7%) doesn't affect the real part of the effective dielectric constant by very much. With only a slight difference in these mixing rules, the required porosity needed in order to decrease the real part of the dielectric constant to 1.45 would only be  $\sim 5\%$  smaller if using the Maxwell-Garnett rule with a vacuum as the host medium or using the Bruggeman mixing rule. Therefore, we would still require the ring particles to have  $\sim 70\%$  porosity when using those two rules.

After obtaining the required real part of the ring particle effective dielectric constant and its corresponding porosity, we are able to derive the radially varying non-icy material fraction merely from the required imaginary part of the effective dielectric constant. Here we compare three cases all of which match the required real part of the effective dielectric constant: (1) the particles are 75% porous and the effective dielectric constant is determined using the Maxwell-Garnett mixing rule with water ice as host medium; (2) the particles are 70% porous and the effective dielectric constant is determined using the Maxwell-Garnett mixing rule with vacuum as host medium; and (3) the particles are

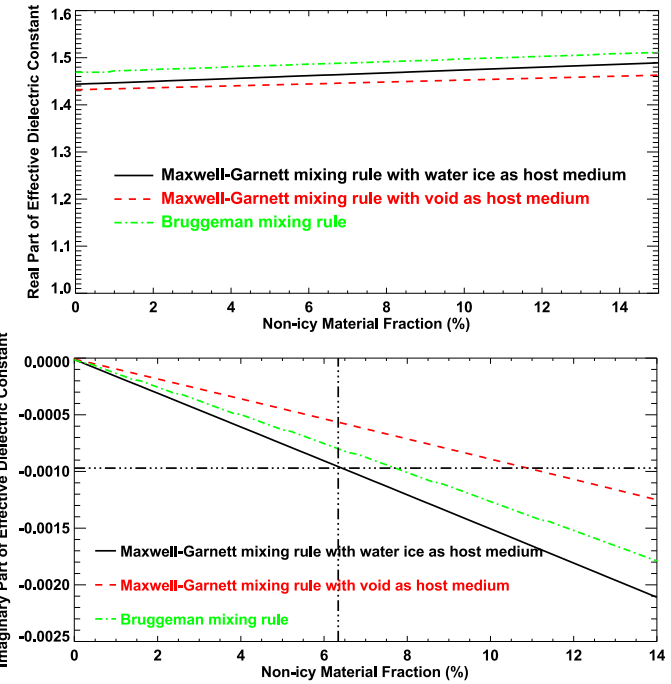


**Fig. 23.** Black curve: Maxwell-Garnett mixing rule with water ice as the host material, and 75% porous C ring particles. Red curve: Maxwell-Garnett mixing rule with vacuum as the host medium, and 70% porous C ring particles. Green curve: Bruggeman mixing rule with 70% porous C ring particles.

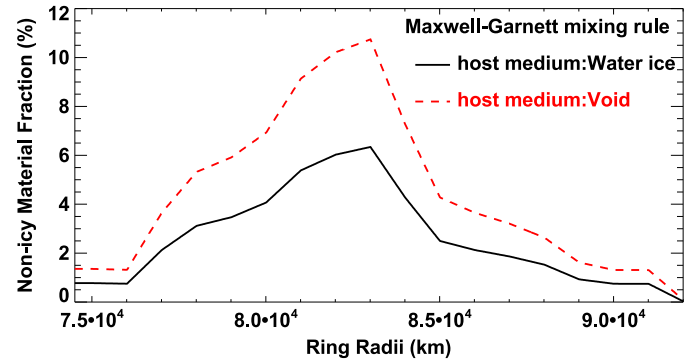


**Fig. 24.** Black curve: Maxwell-Garnett mixing rule with water ice as the host material, and 75% porous C ring particles. Red curve: Maxwell-Garnett mixing rule with vacuum as the host medium, and 70% porous C ring particles.

70% porous and the effective dielectric constant is determined using the Bruggeman mixing rule.

In Fig. 23, upper panel, we show that in all three cases, the real part of the dielectric constant remains relatively unchanged with a value of  $\sim 1.45$  as we add more non-icy material. In the lower panel, we investigate how the imaginary part of the effective dielectric constant, which determines the amount of intrinsic thermal emission, varies with the non-icy material fraction mixed within water ice for these same three cases. We find that when using the Maxwell-Garnett mixing rule, taking water ice or vacuum as the host medium actually makes a factor of  $\sim 1.5$  difference in the required non-icy material fraction. The Bruggeman mixing rule consistently always gives a value in between these two cases. Thus, in order to reach the imaginary dielectric constant required to generate the amount of observed thermal emission, we would require about 50% more non-icy material if using the Maxwell-Garnett mixing rule with vacuum as the host medium (see Fig. 24). These two cases set the upper and lower limit of the non-icy material

fraction in the ring particles. The fraction will lie somewhere in between these limits depending on which mixing rule is used. Taking the non-icy material upper limit, the estimated age of the C ring in, for example, the injected Centaur (diffuse debris clouds) model increases from our previous estimate to  $\sim 30 - 90$  Myr. The mass of the silicates contained in the injected Centaur becomes  $2.7 \times 10^{16}$   $\sim 3.0 \times 10^{16}$  kg, and the size of the Centaur also increases slightly to  $\sim 13 - 20$  km, while all other estimates remain similar to their previous values.

## 6. Conclusions

We have calibrated and analyzed the Cassini Radiometry observations of Saturn's rings. The high brightness temperature in the C ring as seen where the ring obscures the planet suggests a scattering phase function that is much more forward-directed than a Mie phase function. We find that we can obtain a consistent scattering phase function by adding 70–75% porosity to the C ring particles. As a consistency check, we have simulated back scattering in the C ring with these highly porous particles and we find a very low, normalized backscatter cross-section of about 3% in agreement with stringent upper limits reported from Arecibo observations for the C ring (Nicholson et al., 2005). We speculate that it may be possible that ring particles achieve a quasi-equilibrium porous regolith as a result of a balance between impact gardening due to micrometeoroid bombardment, and ballistic transport and inter-particle collisions.

The amount of non-icy material in Saturn's rings is the key to understanding their origin and age, and the Cassini RADAR has, for the first time, provided us with the chance to measure the non-icy material fraction within the bulk of the ring mass in the microwave, which is much more sensitive to the embedded pollutants than visible or near-IR observations. From our analysis, we have determined the non-icy material fraction as a function of radius in the C ring, and find that the non-icy component reaches a maximum of 6–11% by volume in the center of the C ring (when assuming the non-icy material is intramixed with water ice), and the fraction decreases gradually inward and rapidly outward from this radial location. The radial variation of the non-icy material, the concentration of which reaches a maximum near 83,000 km, cannot be explained by direct meteoroid deposition alone.

We have proposed a possible scenario in which a passing Centaur provides the necessary material for post-formation enhancement of the C ring non-icy material in addition to a smaller meteoroid infall component. We have considered two variations of this scenario. First, we suggested that diffuse debris clouds derived from the incoming Centaur, disrupted from previous encounters with the planet or rings, are absorbed and become intramixed with the rings' icy particles. In this case, the currently observed non-icy material distribution of the C ring would have taken some 15–90 Myr to accumulate given the currently accepted value of the micrometeoroid flux at infinity of  $\sim 4.5 \times 10^{-17}$  g cm $^{-2}$  s $^{-1}$ , with the variation in time scale depending on specifics of the treatment of the EMT model, and the non-icy material fraction in the inner and outer C ring as determined by the local opacity. This scenario can explain the high non-icy material fraction, but not the low opacity there. Specifically, we have found that 70–75% porous particles using our nominal particle size distribution for the C ring results in a ring opacity of  $\sim 0.07 - 0.08$  cm $^2$  g $^{-1}$  (see solid curve, Fig. 17), which is a factor of  $\sim 4$  higher than yielded by the density wave measurements in the middle C ring.

As a variant on the Centaur disruption model, we have considered the likelihood that a recently-captured Centaur would not have been ground down to powder, but in fact most of its mass would remain in larger chunks in the cm-m range, which have since acquired porous, icy mantles over time. As a result, we pro-

posed a silicate-core and porous-dirty-icy-mantle model in which the mass of the Centaur is initially contained in a narrow annulus located at the peak of the current non-icy material fraction bump in the C ring center (83,000 km). We have shown that this annulus can viscously spread to the feature's current width and surface density in as little as  $\sim 20 - 30$  Myr, though this depends on model parameters. It is possible that a combination of viscous spreading and ballistic transport acting together could shorten this time further. We find this variant more compelling because it successfully fulfills the requirements for a strong forward-directed scattering phase function, while explaining both our derived radially-variable thermal emission and the low opacity in the middle C ring, without requiring the Centaur to be ground to powder.

We have examined other possible scenarios that might account for the observations, and identified the difficulties with them. We considered the possibility that the silicates in the C ring came from an object that originated from within the Saturnian system. This could have occurred from the breakup of one or more of the Saturnian moons, either from tidal disruption, catastrophic impact by a heliocentric interloper or even a collision between mid-sized satellites. However, such a scenario faces several hurdles, not least of which is that the event must have occurred within the last  $\sim 100$  Myrs. This time scale becomes realizable if the tidal dissipation parameter for Saturn is much lower than previously thought, which remains controversial. Even so, an embedded rocky fragment of the required size that originated from one of these moons would almost certainly have significant strength, and would need to be totally broken up into small chunks via a catastrophic impact with an object of heliocentric origin. In such a case, then it is possible that its evolution could be similar to the Centaur model. However, we have investigated the probability of such a catastrophic impact occurring within the last  $\sim 100$  Myr and have found an optimistic estimate to be on the order of  $\sim 2 - 3\%$ .

We have also considered a scenario in which meteoroid bombardment is the only pollution source, which provides the mid-C-ring non-icy fraction only if the rings formed  $\sim 900$  Myr ago, again assuming a micrometeoroid flux at infinity of  $\sim 4.5 \times 10^{-17}$  g cm $^{-2}$  s $^{-1}$ . But the nearly flat radial distribution of the flux would mean that mechanisms would then need to be identified that would act to dilute or decrease the non-icy material in the inner and outer C ring. Ballistic transport in the outer C ring may act to dilute the non-icy fraction as icy material spills over from the inner B ring over time. However, the inner C ring remains problematic. As a final consideration, we postulate that ring rain erosion would tend to make the non-icy material fraction in the inner and middle C ring higher than the fraction in the outer C ring. That is, the non-icy material fraction in the inner and middle regions would have been increased as ice was preferentially eroded away along magnetic field lines. Given that there are more uncertainties inherent in this scenario, we find the Centaur capture model more preferable. Future observations at the Cassini F-ring and proximal orbits are likely to provide more insight as both passive and active radiometry data with very high resolution will be acquired. The passive observations will cover a wider range of the scattering profile showing its complete shape as well as allowing for the determination of a more detailed profile of the non-icy material fraction, while the active observations will measure the ring particles' backscattering cross sections which are very sensitive to their porosity and composition.

Finally, although we have not specifically addressed the possibility in this paper, it has been proposed that the rings could have been initially much more massive in the past, having formed from the breakup of a large moon (e.g., Charnoz et al., 2009a; Canup, 2010). Such a massive disk would then evolve viscously over time to its current lower-mass state. A difficulty with this scenario is that much of the material may evolve inwards into the C ring

region increasing its surface density considerably relative to the B ring (see [Salmon et al., 2010](#); [Charnoz et al., 2011](#)) which is inconsistent with the rings' current configuration, unless some mechanism can act to prevent or limit inward spreading. If it were the case though, the age of the C ring would likely be older than our estimation, since massive rings would be less vulnerable to pollution by meteoroid impacts and it would take a longer time to reach the non-icy material fraction we observe today. However, given that the low optical depth C ring would take  $\sim 700$  Gyr to double its width by viscous spreading alone ([Charnoz et al., 2009b](#)), it would seem unlikely that the rings have achieved their current configuration this way, if they were indeed initially very massive. Therefore additional mechanism(s) would have to be identified that can explain the C ring's current low mass density and optical depth relative to the B ring. Despite this apparent puzzle, an initially massive ring remains an interesting possibility that is worthy of further study.

## Acknowledgments

We thank NASA Outer Planets Research Program (Grant Number [NNX14AR27G](#)) for funding this work. We thank Luke Dones for providing an estimate for the timescale of catastrophic breakup of Saturnian fragments. We thank Joseph Burns, Matthew Tiscareno and Michael Evans for helpful conversations. Finally we gratefully acknowledge those who designed, developed and operate the Cassini/Huygens mission, which is a joint endeavor of NASA, the European Space Agency (ESA), and the Italian Space Agency (ASI) and is managed by JPL/Caltech under a contract with NASA.

## Appendix A. Correction for radar beam 3 boresight direction update

After investigating the brightness temperature profiles (brightness temperature vs. ring radius) of the occulting rings in our four low-resolution map scans, we uncovered a radial misalignment between profiles from different observations. The misalignment between Rev038\_1\_LOW and Rev038\_2\_LOW is the most significant, being as large as 3000 km (See Fig. A.1, panel 1). As an example, in Fig. A.1, panel 1, we plot the brightness temperature profile of Rev038\_1\_LOW and Rev038\_2\_LOW both at polarization 2, which suggests that this misalignment is not due to particle scattering effects. The brightness temperature profiles of occulting rings from the other two occasions lie in between Rev038\_1\_LOW and Rev038\_2\_LOW (see Fig. A.1, panel 2), which implies that it is not a breakdown on any one particular occasion, but a radial misalignment that exists in all the observations. A possible reason for this misalignment may be a shift of the boresight direction of Radar beam 3 (see below).

The Radar beam 3 boresight axis was designed to lie along the spacecraft  $-Z$  axis and no adjustment to its pointing in the spacecraft coordinates has been reported. However, RSS and RADAR observations share the same physical antenna. The X band and Ka band boresights have been shifted from the spacecraft  $-Z$  axis [0, 0,  $-1$ ] to [0.0004900, 0.0004500,  $-0.9999998$ ] as recorded in the Cassini spacecraft frame definitions kernel. These boresight directions were corrected as a result of RSS radio occultation observations. It is very likely that Radar beam 3, which shares the same receiving feed with X- and Ka-band, requires the same boresight directional shift. Thus, we applied the above updated boresight direction to our calibration and found that it aligned all four brightness temperature profiles (see Fig. A.2).

In Fig. A.2, the observed brightness points are not as perfectly aligned as is any single observation. There are two main reasons for this  $\sim 10$  K spread. First, the slight differences between different

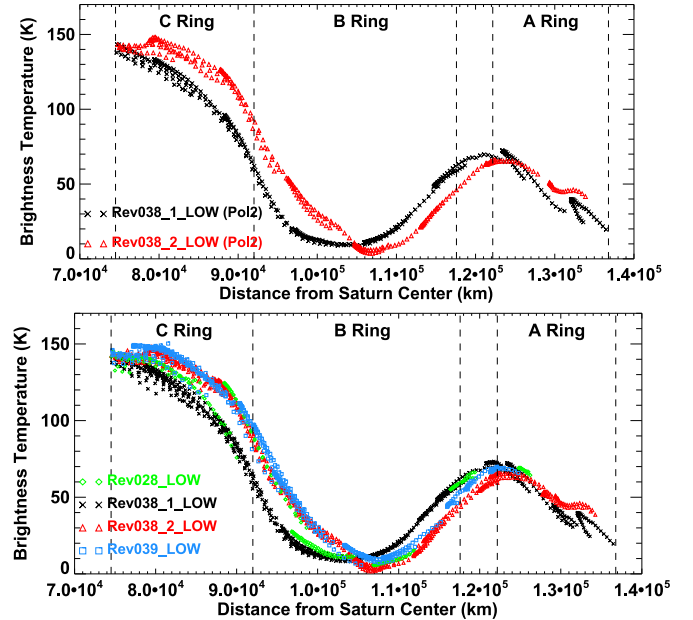


**Fig. A.1.** Brightness temperature profiles (brightness temperature vs. ring radius) of occulting data in low-resolution map scans. Upper panel: The radial misalignment of the brightness temperature profiles between Rev038\_1\_LOW and Rev038\_2\_LOW at polarization 2. Lower panel: the brightness temperature profiles of occultation data from all four low-resolution map-scan occasions. All available polarizations are combined together for each occasion in the lower panel. (For interpretation of the references to colour in this figure legend, the reader is referred to the web version of this article.)

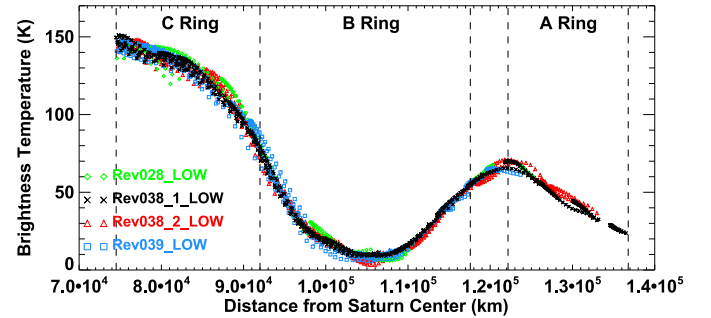


**Fig. A.2.** Brightness temperature profile of occultation data for all four low-resolution scans after applying the boresight correction. These data now coincide with each other quite well. (For interpretation of the references to colour in this figure legend, the reader is referred to the web version of this article.)

occasions may be caused by the change in the Cassini-Saturn distance and in the ring opening angle during different occasions. For example, the smallest Cassini-Saturn distance was 19 Saturn radii for Rev028\_LOW while the largest distance was 24 Saturn radii for Rev038\_1\_LOW. The resolution for Rev028\_LOW is thus 20% higher than that for Rev038\_1\_LOW. Furthermore, the ring opening angle for Rev038\_1\_LOW of  $\sim -18$  to  $-20^\circ$  increases to  $\sim -22$  to  $-25^\circ$  for Rev039\_LOW. A larger ring opening angle will not only lead to a slight increase in the resolution (the radial projection of the beam on the ring layer becomes smaller), but also diminish the transmittance. In the C ring, for example, in regions with optical depth of 0.2, the directly transmitted light increases by 15 K as the ring opening angle increase from  $18$  to  $25^\circ$ . All these differences in geometry may cause small differences in the brightness profiles. Second, in some circumstances, the spread of brightness temperature at a particular ring radius may be due to comparing observations at different azimuthal angles. In the C ring, for example, half of the brightness is contributed by scattered Saturn

radiation and the scattering phase function varies quickly at small scattering angles.

## References

- Altobelli, N., et al., 2015. Dust populations in the outer solar system: 10 years of monitoring by cassini-CDA. In: Proceedings of the EPSC. Nantes, France id.EPSC2015-577.
- Araki, S., Tremaine, S., 1986. The dynamics of dense particle disks. *Icarus* 65, 83–109.
- Asphaug, E., Reufer, A., 2013. Late origin of the saturn system. *Icarus* 223, 544–565.
- Baillie, K., et al., 2011. Waves in cassini UVIS stellar occultations. 2. the c ring. *Icarus* 216.
- Bohren, C., Huffman, D.R., 1983. *Absorption and scattering of light by small particles*. Wiley, New York.
- Bruggeman, D.A.G., 1935. Berechnung verschiedener physikalischer konstanten von heterogenen substanzen. I. Dielektrizitätskonstanten und Leitfähigkeiten der Mischkörper aus isotropen Substanzen. *Annalen der Physik* 416.
- Canup, R.M., 2010. Origin of saturn's rings and inner moons by mass removal from a lost titan-sized satellite. *Nature* 468 (7326), 943.
- Charnoz, S., 2009a. Did saturn's rings form during the late heavy Bombardment? *Icarus* 199 (2), 413–428.
- Charnoz, S., 2009b. Origin and evolution of saturn's ring system. In: Dougherty, M.K., Esposito, L.W., Krimigis, S.M. (Eds.), *Saturn After Cassini-Huygens*. Springer-Verlag Press, pp. 537–576.
- Charnoz, S., et al., 2011. Accretion of saturn's mid-sized moons during viscous spreading of young massive rings: solving the paradox of silicate-poor rings versus silicate-rich moons. *Icarus* 216, 535–550.
- Chesley, S.R., et al., 2002. Quantifying the risk posed by potential earth impacts. *Icarus* 159 (2), 423–432.
- Clark, R.N., et al., 2008. Compositional mapping of saturn's satellite dione with cassini VIMS and implications of dark material in the saturn system. *Icarus* 193, 372–386.
- Clark, R.N., et al., 2012. Nano-Iron on outer solar system Satellites, implications for space weathering. In: Proceedings of the AGU, Fall Meeting #P53B-05.
- Colwell, J.E., et al., 2007. Self gravity wakes and radial structure in saturn's b ring. *Icarus* 190, 127–144.
- Colwell, J.E., et al., 2010. Cassini UVIS stellar occultation observations of saturn's rings. *Astron. J.* 140, 1569–1578.
- Cruikshank, D.P., et al., 2005. Tholins as coloring agents on outer solar system bodies. *Adv. Space Res.* 36, 178–183.
- Cuk, M., 2014. After Imbrium, before Babylon: solar system's middle years. 46th DPS Meeting Urey Prize Lecture.
- Cuk, M., Dones, L., Nesvorný, D., 2016. Dynamical evidence for a late formation of saturn's moons. Submitted to *Astrophys. J.*
- Cuzzi, J.N., Pollack, J.B., 1978. Saturn's rings: particle composition and size distribution as constrained by microwave observations. I - Radar observations. *Icarus* 33, 233–262.
- Cuzzi, J.N., Pollack, J.B., Summers, A.L., 1980. Saturn's rings - Particle composition and size distribution as constrained by observations at microwave wavelengths. II - Radio interferometric observations. *Icarus* 44, 683–705.
- Cuzzi, J.N., et al., 1984. Saturn's rings: properties and processes. In: Greenberg, R., Brahic, A. (Eds.), *Planetary Rings*. University of Arizona Press, Tucson.
- Cuzzi, J.N., Estrada, P.R., 1998. Compositional evolution of saturn's rings due to meteoroid bombardment. *Icarus* 132, 1–35.
- Cuzzi, et al., 2014. Utilitarian opacity model for aggregate particles in protoplanetary nebulae and exoplanet atmospheres. *Astrophysical J. Suppl.* 210 (2) article id. 21.
- Cuzzi, J.N., et al., 2009. Ring particle composition and size distribution. In: Dougherty, M.K., Esposito, L.W., Krimigis, S.M. (Eds.), *Saturn From Cassini-Huygens*. Springer-Verlag Press, p. 459. p. 45.
- Daisaka, H., Ida, S., 1999. Spatial structure and coherent motion in dense planetary rings induced by self-gravitational instability. *Earth, Planet Space* 51, 1195anetar
- Daisaka, H., Tanaka, H., Ida, S., 2001. Viscosity in a dense planetary ring with self-gravitating particles. *Icarus* 154 (2964), 29.
- de Pater, I., Dickel, J.R., 1991. Multifrequency radio observations of saturn at ring inclination angles between 5 and 26 degrees. *Icarus* 94, 474.
- Di Sisto, R.P., Brunini, A., 2007. The origin and distribution of the centaur population. *Icarus* 190, 224–235.
- Dones, L., 1991. A recent cometary origin for saturn's rings? *Icarus* 92, 194.
- Dones, L., 1993. Voyager photometry of saturn's a ring. *Icarus* 105, 184–215.
- Dougherty, et al., 2009. *Saturn from Cassini-Huygens*. Springer ISBN 978-1-4412-0216-9.
- Dunn, D.E., et al., 2002. More microwave observations of Saturn: modeling the ring with a monte carlo radiative transfer code. *Icarus* 160, 132.
- Dunn, D.E., 2004. Microwave observations of saturn's rings: anisotropy in directly transmitted and scattered saturnian thermal emission. *Icarus* 171.
- Dunn, D.E., et al., 2005. High-Quality BIMA-OVRO images of saturn and its rings at 1.3 and 3 millimeters. *Astron. J.* 129, 1109.
- Durisen, R.H., 1992. Ballistic transport in planetary ring systems due to particle erosion mechanisms. II - Theoretical models for saturn's A- and B-ring inner edges. *Icarus* 100.
- Elachi, C., 2004. RADAR: the cassini titan radar mapper. *Space Sci. Rev.* 115, 71–110.
- Elliott, J.P., Esposito, L.W., 2011. Regolith depth growth on an icy body orbiting saturn and evolution of bidirectional reflectance due to surface composition changes. *Icarus* 212.
- Esposito, L.W., 1984. Saturn's rings: Structure, dynamics, and particle properties. In: Gehrels, T., Matthews, M. (Eds.), *Saturn*. University of Arizona Press, Tucson.
- Esposito, L.W., 2008. History of saturn's rings from UVIS observations. In: Proceedings of the EPSC, p. 757.
- Estrada, P.R., Cuzzi, J.N., 1996. Voyager observations of the color of saturn's rings. *Icarus* 122, 251–272.
- Estrada, P.R., et al., 2015. Combined structural and compositional evolution of planetary rings due to micrometeoroid impacts and ballistic transport. *Icarus* 252, 415–439.
- French, R.G., Nicholson, P.D., 2000. Saturn's rings II. particle sizes inferred from stellar occultation data. *Icarus* 145, 502–523.
- French, R.G., et al., 2007. HST observations of azimuthal asymmetry in saturn's rings. *Icarus* 189, 493–522.
- Goldreich, P., Tremaine, S., 1978. The velocity dispersion in Saturn's rings. *Icarus* 34, 227.
- Goldreich, P., Tremaine, S., 1982. The dynamics of planetary rings. *Ann. Rev. Astron. Astrophys.* 20, 249–283.
- Grossman, A.W., 1990. *Microwave Imaging of Saturn's Deep Atmosphere and Rings*. Unpublished Ph.D. thesis. California Institute of Technology, Pasadena.
- Hanel, R., 1981. Infrared observations of the saturnian system from voyager 1. *Sci.(80- )* 212, 192–200.
- Hanel, R., 1982. Infrared observations of the saturnian system from voyager 2. *Sci. (80- )* 215, 544–548.
- Harbison, R.A., 2013. The smallest particles in saturn's a and c rings. *Icarus* 226 (2).
- Harris, A.W., et al. The origin and evolution of planetary rings. IN: *Planetary rings* (1984)
- Hedman, M.M., 2011. Saturn's curiously corrugated c ring. *Sci. (80- )* 332 (6030).
- Hedman, M.M., Nicholson, P.D., 2013. Kronoseismology: using density waves in saturn's c ring to probe the planet's interior. *Astronomical J.* 146.
- In press at Icarus. arxiv: Hedman, M.M., Nicholson, P.D. The B-ring's surface mass density from hidden density waves: less than meets the eye?
- Horner, J., 2004. Simulations of the population of centaurs I: the bulk statistics. *Mon Not R Astron Soc* 354 (3).
- Hyodo, R., Ohtsuki, K., 2014. Collisional disruption of gravitational aggregates in the tidal environment. *Astrophys. J.* 787, 56 (May).
- Janssen, M.A., et al., 2009. Titan's surface at 2.2-cm wavelength imaged by the cassini radar radiometer: calibration and first results. *Icarus* 200 (1) titan.
- Janssen, M.A., et al., 2013. Saturn's thermal emission at 2.2-cm wavelength as imaged by the cassini RADAR radiometer. *Icarus* 226 (1).
- Janssen, M.A., et al., 2016. Titan's surface at 2.2-cm wavelength imaged by the cassini RADAR radiometer: results and interpretations through the first ten years of observation. *Icarus*, in press doi:10.1016/j.icarus.2015.09.027.
- Johnston, W.R., 2015. TNO and centaur diameters, albedos, and densities V3.0. *EAR-A-COMPIL-5-TNOCENALB-V3.0*. NASA Planetary Data System.
- Jontof-Hutter, D., Hamilton, D.P., 2012a. The fate of sub-micron circumplanetary dust grains I: aligned dipolar magnetic fields. *Icarus* 218 (1).
- Jontof-Hutter, D., Hamilton, D.P., 2012b. The fate of sub-micron circumplanetary dust grains II: multipolar fields. *Icarus* 220 (2).
- Kofman, W., et al., 2015. Properties of the 67P/Churyumov-Gerasimenko interior revealed by CONCERT radar. *Sci. (80- )* 349 (6247).
- Lainey, V., et al., 2010. Saturn tidal dissipation from astrometric observations. In: Proceedings of the EPSC. Rome, Italy, p. 123.
- Lainey, V., et al., 2012. Strong tidal dissipation in saturn and constraints on Enceladus' thermal state from astrometry. *Astrophys. J.* 752.
- Larsen, J.A., et al., 2001. The spacewatch wide-area survey for bright centaurs and trans-neptunian objects. *Astron. J.* 121, 562–579.
- Leinhardt, Z.M., Stewart, S.T., 2009. Full numerical simulations of catastrophic small body collisions. *Icarus* 199.
- Marouf, E.A., 2008. *Saturn After Cassini-Huygens*, conference #113.
- Marouf, E.A., et al., 2011. Uncovering of small-scale quasi-periodic structure in saturn's c ring and possible origin. In: EPSC-DPS joint meeting, Oct 2–7. Nantes, France, p. 265.
- Mishima, O., 1983. The far-infrared spectrum of ice Ih in the range 8–25 cm<sup>-1</sup>. Sound waves and difference bands, with application to saturn's rings. *J. Chem. Phys.* 78 (11), 6399–6404.
- Morfill, G.E., 1983. Some consequences of meteoroid bombardment of saturn's rings. *Icarus* 55, 439–447.
- Morishima, R., et al., 2016. Incomplete cooling down of saturn's a ring at solar equinox: implication for seasonal thermal inertia and internal structure of ring particles. *Icarus* in press.
- Morris, R.V., 1985. Spectral and other physiochemical properties of submicron powders of hematite (-Fe2O3), maghemite (-Fe2O3), maghemite (Fe3O4), goethite (-FeOOH), and lepidochrosite (-FeOOH). *J. Geophys. Res.* 90, 3126–3144.
- Nicholson, P.D., 2005. Radar imaging of saturn's rings. *Icarus* 177 (1).
- Nicholson, P.D., 2008. A close look at saturn's rings with cassini VIMS. *Icarus* 193 (1).
- Nicholson, P.D., Hedman, M.M., 2010. Self-gravity wake parameters in saturn's a and b rings. *Icarus* 206 (2).
- Porco, C.C., et al., 2008. Simulations of the dynamical and light-scattering behavior of saturn's rings and the derivation of ring particle and disk properties. *Astron. J. (N.Y.)* 136, 2172–2200.
- Poulet, F., Cuzzi, J.N., 2002. The composition of saturn's rings. *Icarus* 160, 350–358.
- Poulet, F., 2003. Compositions of saturn's rings A, B, and C from high resolution near-infrared spectroscopic observations. *Astron. Astrophys.* 412, 305–316.
- Pringle, J.E., 1981. Accretion discs in astrophysics. *Ann. Rev. Astron. Astrophys.* 19, 137–162.

- Reffet, E., 2015. Thickness of saturn's b ring as derived from seasonal temperature variations measured by cassini CIRS. *Icarus* 254.
- Salmon, J., et al., 2010. Long-term and large-scale viscous evolution of dense planetary rings. *Icarus* 209, 771–785.
- Salo, H., 1992. Gravitational wakes in saturn's rings. *Nature* 359, 619–621.
- Schmidt, J., et al., 2009. Dynamics of saturn's dense rings. In: Dougherty, M.K., Esposito, L.W., Krimigis, S.M. (Eds.), *Saturn After Cassini-Huygens*. Springer-Verlag Press, p. 413. p. 41.
- Sierks, et al., 2015. On the nucleus structure and activity of comet 67P/Churyumov-Gerasimenko. *Sci. (80- )* 347 (6220).
- Smith, B.A., 1982. A new look at the saturn system – The Voyager 2 images. *Sci. (80- )* 215.
- Stillman, D., Olhoeft, G., 2008. Frequency and temperature dependence in electromagnetic properties of martian analog minerals. *J. Geophys. Res.* 113 (E9).
- Thomas, P.C., 2007. Hyperion's sponge-like appearance. *Nature* 448, 50–56.
- Johnson, T.V., Lunine, J.I., 2005. Saturn's moon phoebe as a captured body from the outer solar system. *Nature* 435 (7038).
- Tsiganis, K., et al., 2005. Origin of the orbital architecture of the giant planets of the solar system. *Nature* 435, 459–461.
- van der Tak, et al., 1999. Time variability in the radio brightness distribution of saturn. *Icarus* 142, 125.
- Zahnle, K., et al., 2003. Cratering rates in the outer solar system. *Icarus* 163.
- Zebker, H.A., Marouf, E.A., Tyler, G.L., 1985. Saturn's rings: Psarticle size distributions for thin layer model. *Icarus* 64 (5314), 53.